METABOLIC ADAPTATIONS TO NEURONAL ACTIVITY IN THE MEDIAL NUCLEUS OF THE TRAPEZOID BODY

NICOLA PALANDT

Dissertation at the
Graduate School of Systemic Neurosciences
Ludwig-Maximilians-Universität München

Munich, 27. April 2023

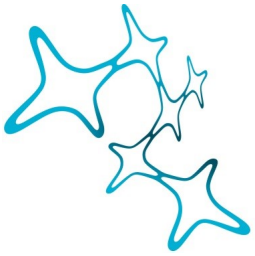

Graduate School of
Systemic Neurosciences
LMU Munich

Dissertation at the
Graduate School of Systemic Neurosciences
Ludwig-Maximilians-Universität München

METABOLIC ADAPTATIONS TO NEURONAL ACTIVITY IN THE MEDIAL NUCLEUS OF THE TRAPEZOID BODY

Submitted by
NICOLA PALANDT
Munich, 27. April 2023

SUPERVISOR AND FIRST REVIEWER
PD Dr. Lars Kunz
Division of Neurobiology
Faculty of Biology
Ludwig-Maximilians-Universität München

SECOND REVIEWER
PD Dr. Conny Kopp-Scheinpflug
Division of Neurobiology
Faculty of Biology
Ludwig-Maximilians-Universität München

EXTERNAL REVIEWER
Prof. Dr. Oliver Kann
Division of Allgemeine Neurophysiologiy
Institut for Physiology und Pathophysiologie
Universität Heidelberg

DATE OF SUBMISSION: 27. April 2023

DATE OF DEFENSE: 14. September 2023

ABSTRACT

The transmission of neuronal signals comes with a high energy cost. Restoring the membrane potential and recycling of synaptic vesicles results in substantial consumption of ATP. To manage these temporal peaks in energy demand, neurons likely adapt their metabolism. Depending on neuron type and firing frequencies, the energy consumption varies; therefore, different adaptations are possible.

In my doctoral research, I tracked the levels of NADH and FAD by imaging their autofluorescence, as well as the levels of extracellular oxygen with an electrochemical electrode. NADH and FAD are two important cofactors involved in core metabolic pathways such as cellular respiration. Tracking the levels of these cofactors together with the oxygen consumption helps to gain valuable insights which metabolic pathways are used for ATP generation. I used such measurements to explore the impact of different firing frequencies, different firing patterns and glucose concentrations on the used metabolic pathways and possible adaptations. The principal neurons of the medial nucleus of the trapezoid body (MNTB) were stimulated electrically at the fibre tract with a broad frequency range. The MNTB in the auditory brainstem is a suitable nucleus for this study since it contains neurons that are able to fire in a broad frequency range, up to 1000 Hz. I also attempted to establish an ATP FRET sensor in the Mongolian gerbil using a systemic virus application for the first time. This allows to obtain more direct information about the brain's energy pathways and extends the autofluorescence study with these informations. Finally, I developed a model that allows a better interpretation of the experimental data and to find worthy research directions.

The electrical stimulation with different frequencies resulted in a strong increase in NADH and FAD peak amplitude, when elevating the frequency from 10 to 100 Hz. At higher frequencies and a fixed number of stimuli, the amplitude of autofluorescence as well as of O_2 decreased again. This suggests that MNTB neurons undergo a metabolic switch from oxidative

phosphorylation during low firing frequencies to glycolysis at high firing frequencies. An increase of extracellular glucose concentration from 2 mM to 10 mM showed a decrease in FAD amplitudes and NADH overshoot pointing to a switch from oxidative phosphorylation towards more glycolysis. Even though I could not fully establish an ATP FRET sensor for further analysis, I achieved an expression of the sensor with a systemic application of AAV-PHP.eB in the Mongolian gerbil. With this, it is possible to use a different model organism than mice or rats. The mathematical model provides a promising framework for further investigation into the energy demands of MNTB neurons.

CONTENTS

1

INTRODUCTION

1.1 METABOLISM OF NEURONS

Neurons have an extremely high energy consumption. Disturbances in metabolism, and consequently in energy supply, may lead to the occurrence of neurodegenerative diseases. Neurons require energy in the form of adenosine triphosphate (ATP) not only for 'housekeeping' processes but also to maintain their membrane potential. Additionally, neurons expend considerable energy for the transmission of signals, which is the main purpose of neurons. Every action potential (AP) disturbs the resting potential of the cell by the influx of Na^+ and the outflux of K^+ ions. The necessary ionic gradient needs to be rescued in a short period of time by the Na^+-K^+ pump under ATP consumption. Also in the synapse, ATP is crucial to pack vesicles with neurotransmitters for the transmission to the next neuron. This is one reason why it is estimated that neurons consume 70-80% of the total brain energy (Camandola and Mattson, 2017, Forderhase et al., 2020). Around 55% of the neuronal energy is consumed by the axonal terminals where not only the membrane pumps (Na^+-K^+-ATPase, Ca^{2+}-ATPase) need to be sustained but also the synaptic vesicle recycling (Li and Sheng, 2022). It is estimated that the recycling of one glutamate vesicle needs more than 20 000 ATP molecules (Li and Sheng, 2022).

A disturbance in brain metabolism can lead to neurodegenerative diseases such as Alzheimer, Parkinson or Huntington's disease (Kuhl et al., 1984, Hoyer, 1991, Camandola and Mattson, 2017, Mayorga-Weber et al., 2022). For example, patients with Alzheimer's disease have fewer glucose transporters that are important for glucose uptake and also a loss of activity for

several important enzymes of the glycolysis was shown (Camandola and Mattson, 2017). For this reason, it is important to understand the metabolism of neurons and investigate their energetic adaptations. Additionally, a better understanding of the metabolism of neurons will help to improve interpretations of brain imaging data such as functional magnetic resonance imaging (fMRI), that try to map changes in blood flow to neuronal activity.

1.1.1 *The Fuel of Neurons*

Neurons can metabolise different substrates. It is highly debated which substrate is the most important for neurons (glucose or lactate) (Castro et al., 2009, Dienel, 2019, Jha and Morrison, 2018). In the following section, the three most important fuels for neuron energy metabolism are introduced.

Glucose

Glucose is the main fuel for the brain (Mergenthaler et al., 2013, Dienel, 2019). With glucose transporter 1 (GLUT1) it crosses the blood-brain barrier to the extracellular fluid from where neurons can take up glucose with GLUT3, which is a more efficient GLUT (Mergenthaler et al., 2013, Jha and Morrison, 2018). In the cytosol, glycolysis can produce pyruvate from glucose under NAD^+ reduction to generate ATP (Fig. 1.1). The mitochondria take up the produced pyruvate, which is the needed fuel for the tricarboxylic acid (TCA) cycle. In the TCA cycle, NADH and $FADH_2$ are produced, the two important dinucleotides for oxidative phosphorylation (OxPhos). In the mitochondrial matrix, OxPhos generates an H^+ gradient by consuming NADH and $FADH_2$ along with oxygen. This gradient drives ATP production by feeding into the ATP synthase. The OxPhos is a multifold more efficient pathway for the synthesis of ATP compared to glycolysis but an oxygen supply is necessary (Berg et al., 2018).

Lactate

Besides glucose as fuel, neurons are able to metabolise lactate for ATP generation (Jha and Morrison, 2018). Monocarboxylic acid transporters (MCTs) can take up lactate from the extracellular space. Afterwards, it can be transformed into pyruvate under NAD^+ reduction by the lactate dehydrogenase (LDH), fueling the TCA cycle. The sources of lactate are

often astrocytes and oligodendrocytes that take up and metabolise a lot of glucose (Jha and Morrison, 2018). Astrocytes and oligodendrocytes use the glucose in two ways 1) producing glycogen for storage and 2) producing lactate from pyruvate (Dienel, 2019, Magistretti and Allaman, 2015, Jha and Morrison, 2020). The astrocytes release the lactate through MCTs into the extracellular space, where it can be taken up by the neurons. According to the lactate shuttle hypothesis, this additional lactate is important for neurons to sustain their great energy consumption (Pellerin and Magistretti, 1994, Castro et al., 2009, Magistretti and Allaman, 2015, Jha and Morrison, 2018, 2020, Zuend et al., 2020) (more details in section 1.3.1). In the dorsal striatum, it was shown that under stimulation both lactate and glucose levels were increasing in the extracellular space followed by a strong dip in glucose levels and later a smaller dip in lactate levels (Forderhase et al., 2020). Experiments of Baeza-Lehnert et al. (2019) showed that the glucose consumption of resting neurons increased to the double if no lactate is present. This leads to the assumption that 50% of the fuel of a resting neuron comes from lactate. Although lactate seems to be a good substrate, Hollnagel et al. (2020) demonstrated that lactate on its own is not sufficient to fuel gamma oscillations of pyramidal cells and GABAergic interneurons. It leads to reduced neurotransmitter release and attenuates synaptic transmission.

Ketone Bodies

As additional substrate during very limited glucose availability, ketone bodies such as 3-β-hydroxybutyrate (3HB) and acetoacetate (AcAc) were shown to be metabolised (Camandola and Mattson, 2017). This happens during brain development, starvation or fasting periods. In the brain, only astrocytes are able to generate ketone bodies from fatty acids, but they have only low transport rates. For this reason, neurons rely on ketone bodies that are produced by the liver and distributed through the blood. Ketone bodies can be taken up via MCTs by all brain cells. In the mitochondria, it can be converted into acetyl-CoA that feeds the TCA cycle (Mayorga-Weber et al., 2022, Camandola and Mattson, 2017). Ketogenic diets can have a beneficial effect on patients with memory impairment such as found in Alzheimer's disease (Descalzi et al., 2019). Also for epilepsy patients, a 50% reduction of seizures was shown (Vining, 1999, Pan et al., 2019).

1.2 REGULATION OF GLYCOLYSIS AND OXIDATIVE PHOSPHORYLATION

How does the cell know that ATP is needed? In most eukaryotic cells the need for ATP is regulated by the cytosolic ratio of ATP and ADP. A decrease in its ratio leads to an increase in the flux of the respiratory chain and the TCA cycle in the mitochondria and with it the oxygen consumption rises (Hayakawa et al., 2005). In neurons, oxygen consumption was shown to start without a detectable delay (Hayakawa et al., 2005). Moreover, Baeza-Lehnert et al. (2019) could not measure a change in cytosolic ATP/ADP ratio when stimulating the cells. This indicates the existence of a faster mechanism than the regulation by ATP/ADP ratio.

1.2.1 *Regulation by Ca^{2+}*

A faster regulation than the ATP/ADP ratio works through the Ca^{2+} concentration in the cell. In many cell types, an increase of free cytosolic Ca^{2+} results in a decrease of the mitochondrial membrane potential caused by permeation through Ca^{2+} uniporter. This depolarisation of the mitochondrial membrane facilitates the oxidation of NADH to produce ATP and activates different dehydrogenases in the TCA cycle (Hayakawa et al., 2005, Berndt et al., 2015, Díaz-García et al., 2021). Stimulation of neurons by increasing the extracellular K^+ concentration or by electrical stimulation leads to an increase in intracellular Ca^{2+} concentration and the depolarisation of the mitochondrial membrane and within 0.2 seconds (s) the oxygen consumption increases (Duchen, 1992, Hayakawa et al., 2005). An increase in cytosolic Ca^{2+} levels can also be associated with an increase in glycolysis. Bak et al. (2009) showed an increased glucose consumption by superfusion of N-methyl-D-aspartate (NMDA), which results in an increase of cytosolic Ca^{2+} and an increased glucose uptake. On the other hand, Díaz-García et al. (2021) and Meyer et al. (2022) could not find a relation between the Ca^{2+}/calmodulin signalling pathway and the rise of cytosolic NADH after acute stimulation. However, a stimulation also increases cytosolic Na^+ levels, the Na^+-K^+-pump tries to restore the level under ATP consumption and the cytosolic NADH concentration increases. This let them conclude that the glycolysis is mainly triggered by the energy demand of the Na^+-K^+ pump.

Baeza-Lehnert et al. (2019) postulated that the Na^+-K^+-pump as an ATP-sink regulates the mitochondrial ATP production during moderate neuronal activity because they found a strong correlation between Na^+-pumping and ATP production. How exactly this regulation is working remains unclear. One suggested possibility is that the pump might modulate the mitochondria via hexokinase, which is attached to the mitochondria and interacts with several proteins, like the adenine nucleotide translocator (ANT).

1.2.2 *Crabtree, Pasteur and Warburg effect*

In addition to these mechanisms, the metabolic regulation of astrocytes includes well known effects, namely the Crabtree effect, Pasteur effect, and Warburg effect (Barros et al., 2021). The Crabtree effect is the inhibition of OxPhos by an increased glycolysis, which can be a result of increased glucose availability (Barros et al., 2021), or it can be triggered by extracellular K^+ concentration (Fernández-Moncada et al., 2018). The Pasteur effect in contrast is the inhibition of the glycolysis by the mitochondrial metabolism, while the Warburg effect describes the suppression of the Pasteur effect. In astrocytes, neuronal activity leads to a fast Crabtee effect triggered by K^+ and a fast Warburg effect (Barros et al., 2021). The suppression of the OxPhos in astrocytes leads to an increased glycolysis, that produces a lot of lactate. According to the lactate shuttle hypothesis (1.3.1 Lactate shuttle hypothesis) the surplus lactate is shuttled over to neurons.

1.3 METABOLIC ADAPTATIONS

As previously mentioned, one of the main reasons for the high energy demand of neurons is due to the ion pumps and the synaptic vesicle recycling during the transmission of signals. During such a transmission the energy demand rapidly rises for a short period. To ensure a continuous and adequate energy supply, it is likely that neurons have developed metabolic adaptions. These adaptions can differ between brain regions and neuron types since the energy demand varies (Sokoloff, 1981).

1.3.1 *Lactate shuttle hypothesis*

The most popular hypothesis is the lactate shuttle. This hypothesis was first postulated by Pellerin and Magistretti (1994). According to the lactate shuttle hypothesis, astrocytes do consume a lot of glucose to produce lactate that is shuttled to the extracellular space to support neurons during firing (see 1.1.1 The Fuel of Neurons). The additional lactate can be used as substrate for the TCA cycle to produce electron carriers for the electron transport chain (ETC). Supporters of the hypothesis suggested that the glycolysis and the OxPhos are compartmentalised in different cell types and mainly astrocytes and oligodendrocytes metabolise glucose to produce lactate, one of the main sources for neurons (Pellerin and Magistretti, 1994, Jha and Morrison, 2018).

What speaks against this strict understanding of the lactate shuttle is that neurons do express all proteins that are necessary for the glycolysis and have even higher mRNA expression levels than astrocytes for most glycolytic enzymes (Yellen, 2018). Moreover, Bak et al. (2009) demonstrated in cultured neurons that the glucose metabolism is enhanced during neurotransmission while lactate metabolism remains stable. Finally, lactate metabolism could only rarely be linked to physiological neuronal activity, since most studies supporting the lactate shuttle use immature dissociated cell cultures, excessive lactate concentrations, anaesthesia or artificial electrical stimuli (Hollnagel et al., 2020).

Still, many experiments indicate that the lactate shuttle exists. Zuend et al. (2020) for instance showed that an increase of cortical activity triggered by an induced arousal increased extracellular lactate levels while the lactate levels in astrocytes showed a prominent dip. Other studies found an impairment of learning and long-term memory when the uptake of lactate through MCTs was inhibited (Descalzi et al., 2019, Jha and Morrison, 2020)

In conclusion, it is likely that neurons consume both glucose and lactate to sustain their high energy demand. The question of how important the lactate shuttle is depends on the brain region and the energy demand of the different neuron types.

1.3.2 *Energy storage*

The main energy storage in the brain is glycogen, but it occurs mainly in astrocytes. Glycogen can be converted into glucose-6-phosphate very fast without ATP consumption (Dienel, 2019, Bélanger et al., 2011). Although neurons themselves have no glycogen stores, they possibly have an energy storage of phosphocreatine. During deprivation of oxygen and glucose, phosphocreatine can compensate for the lack of ATP, e.g. during a stroke, phosphocreatine storages can regenerate ATP, but only for a limited time (Balestrino et al., 2002, Rackayova et al., 2017). Although creatine, which is a hydrophilic molecule, is barely able to cross the blood-brain-barrier (BBB), Balestrino et al. (2002) were able to show that high doses increase the cerebral phosphocreatine *in vivo*. *In vitro* creatine was able to delay anoxic depolarisation (Balestrino et al., 2002). The importance of this pathway is also demonstrated by the fact that schizophrenia and depression can be associated with disturbed levels of phosphocreatine and creatine (Rackayova et al., 2017).

1.3.3 *Metabolic switch*

Depending on the energy demand, neurons can switch between different pathways for the optimal energy supply (Cerdán et al., 2006, Castro et al., 2009). Different pathways have different advantages and disadvantages. The glycolysis produces only 2 ATPs per glucose but it is extremely fast and does not rely on oxygen. The OxPhos on the other hand is multifold more efficient but it relies on oxygen supply.

Castro et al. (2009) suggested a switch from glycolysis to lactate transport modulated by ascorbic acid. During activation of glutamatergic neurons, glutamate stimulates ascorbic acid release from astrocytes. The ascorbic acid is taken up by neurons, where it is inhibiting glucose transport and stimulates lactate uptake (Castro et al., 2009).

A possible metabolic switch is the aspect that I mainly tried to address with my experiments and analysis. In this thesis, it is shown that a metabolic switch can also happen under high frequency stimulation.

1.4 NEUROENERGETICS IN THE SUPERIOR OLIVARY COMPLEX

The superior olivary complex (SOC) in the auditory brainstem is an interesting system to study the energy metabolism of neurons and has several advantages. Compared to other brain regions the neurons here are extremely energy demanding (Sokoloff, 1981). Medial superior olive (MSO) and lateral superior olive (LSO) neurons for example are extremely leaky and already have a high ATP consumption for keeping the membrane potential (Trattner et al., 2013). All SOC nuclei have high firing frequencies which also costs a lot of energy (Howarth et al., 2012, Brosel et al., 2018). Trattner et al. (2013) quantified different metabolic markers such as glucose transporter 3 (GLUT3), mitochondria and Na+/K+ ATPase with immunohistochemical methods. They showed the increase of these markers during development and the differences between the three SOC nuclei: LSO, MSO and medial nucleus of the trapezoid body (MNTB). In addition to this quantification, they calculated the ATP consumption of the neurons for each nucleus. They concluded that the MSO has the highest energy consumption, while the MNTB has a smaller ATP consumption but reaches its maximum already before hearing onset. Brosel et al. (2018) showed the increased energy demand of LSO neurons by comparing their energy consumption with neurons from the cerebral cortex and the hippocampus CA1. This high energy demand of SOC neurons suggests that metabolic adaptations may have developed in these neurons. Another big advantage is the homogenity of the neurons in the SOC nuclei (Hoffpauir et al., 2010, Brosel et al., 2018). In contrast to other brain regions, the nuclei of the SOC have a homogenous neuronal population that make experiments more comparable and also the interpretation is easier.

1.4.1 *The medial nucleus of the trapezoid body (MNTB)*

The Function of the nucleus

There are two cues that the brain uses to determine the direction of sound: the interaural time and the interaural level difference (ITD and ILD) (Grothe et al., 2010). ILDs define the amplitude difference of the sound wave reaching the two ears occurring by the head that creates an acoustic shadow.

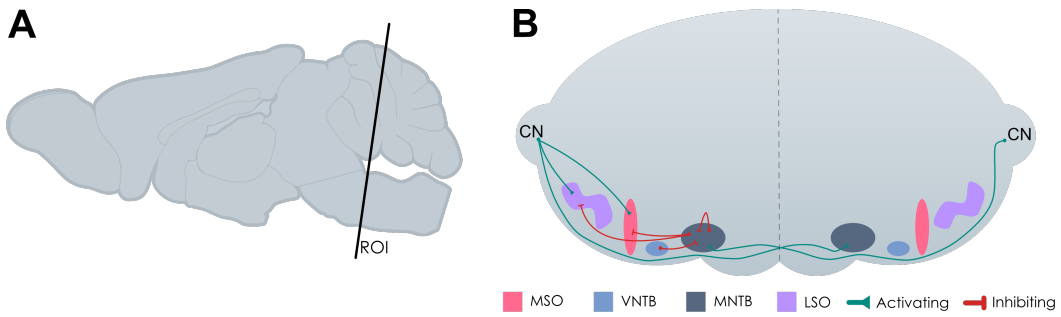

Figure 1.1: Schematic of Superior Olivary Complex (SOC) region *(A) The brain with the cutting angle at the area of the SOC. (B) A brain slice containing the SOC nuclei (Lateral Superior Olive (LSO), Medial Superior Olive (MSO), Ventral Nucleus of the Trapezoid Body (VNTB) and Medial Nucleus of the Trapezoid Body(MNTB)) and the connections of these nuclei with the MNTB. Adapted from Palandt et al. (2023)*

For both cues, the medial nucleus of trapezoid body (MNTB) is important for the processing of directional hearing. The MNTB is part of the SOC. It gets input directly from the globular bushy cells (GBCs) of the cochlear nucleus (CN) that is connected to the auditory nerve (Grothe et al., 2010). The GBCs axons have a high conduction velocity due to their strong mylination and their well defined internodal length (Ford et al., 2015). This leads to a fast transmission from the cochlear nucleus to the contra-lateral MNTB. The GBCs end in huge synapses - the calyces of Held - that completely surround the principal neurons of the MNTB. These gigantic calyces are sufficient to trigger an AP in the principal neurons on their own and thereby minimise the jitter in arrival time (Borst and Soria Van Hoeve, 2012). The principal cells of the MNTB are only slightly slower than the GBCs with a minimum response latency of 3-5 ms. They give glycinergic input to several SOC nuclei and inhibit neurons in the LSO, MSO and ventral nucleus of the trapezoid body (VNTB) (Fig 1.1). In the LSO the level difference is finally computed, while the MSO extracts differences in the arrival time of the sound from the two ears (Grothe et al., 2010). For this processing, extreme precision and accuracy is crucial.

Special biophysics

To achieve the needed precision, the MNTB is extremely special in its biophysics. Many anatomists are interested in the calyx of Held, the giant

synapse that surrounds the big MNTB neurons (Borst and Soria Van Hoeve, 2012). This huge synapse has the advantage of a large number of release sites, a large readily releasable vesicle pool, a low release probability and a large quantal size to assure extreme precision and accuracy for transmission with high firing rates up to 1000 Hz (Kopp-Scheinpflug et al., 2003, Borst and Soria Van Hoeve, 2012). This huge synapse also needs to sustain its energy consumption for the vesicle replenishment. The energy sources of the calyx were researched by some groups (see 1.4.1 Energetics of the calyx).

Also the principal neurons itself are special to enable such a fast transmission. The AMPA glutamate receptors receiving the signal on the post-synaptic site show a fast gating (Borst and Soria Van Hoeve, 2012). Furthermore, a specific form of K^+-channels (K_v3-channels) is expressed in these neurons and are able to minimise AP duration (Wang et al., 1998, Choudhury et al., 2020). All together this allows the MNTB to have one of the highest firing rates in the whole brain and metabolic adaptations are likely to be found here. As comparison, while the MNTB can fire with a frequency up to 1000HZ, in the cortex of mice the highest possible firing rates are around 500Hz (Wang et al., 2016), but typical firing rates in the cortex or hippocampus are around 1 Hz (Vijayan et al., 2010, Hirase et al., 2001). Additional to these high firing rates the MNTB is a nucleus with a homogenous neuron population (Hoffpauir et al., 2010). Experiments like the here described imaging approach average over a neuron population. With a homogenous population statements about a single neuron type are possible instead of averaging over several different neuron types.

Energetics of the calyx

As mentioned the calyx itself has a high energy consumption, because it is such a huge synapse that is able to have one of the highest firing rates in the brain. In literature, there are only a few studies that researched the energy pathways of the calyx. Lucas et al. (2018) described that the calyx consumes glucose and lactate as substrate. A reduction of these substrates reduces the number of functional release sites but changes little in the release probability. By investigating which pathways the calyx uses, the group of Robert Renden found a change during aging and a difference between high and low frequencies. For lower frequencies (0.1 Hz) mainly the glycolysis is important to fuel the ion pumps in the synapse (Lujan et al., 2016). In

young animals (before hearing onset) the energy for higher frequencies (100 Hz) is also sustained by the glycolysis. This is in contrast to older animals (after hearing onset), their ATP production for higher frequencies (300 Hz) relies mainly on the OxPhos (Lujan et al., 2021).

There is nothing found in literature about the major energy pathways of the MNTB neurons itself. With my doctoral research, I investigated the energy pathways of the principal MNTB neurons. The findings about the calyx of Held help to better understand the autofluorescence recordings presented here.

1.4.2 *Model Organism: Meriones unguiculatus*

The Mongolian gerbil *Meriones unguiculatus* is a model organism for ischemia/stroke, epilepsy, aging, visual and auditory research. The similar audiogram of Mongolian gerbils compared to humans makes the gerbil a better auditory model organism than rats or mice that lack the hearing of low frequencies (Cheng et al., 2019, Ryan, 1976). On the other hand are Mongolian gerbils as desert animals very specialised on water deprivation and with this they have metabolic differences compared to non-desert animals. Also their high body temperature of 39°C makes their metabolism different since reactions increase their velocity at higher temperatures, this needs to be kept in mind.

The fact that Mongolian gerbils often evolve epilepsy makes them a good model to investigate this disease. As mentioned earlier is epilepsy a disease where the metabolism of the neurons is disturbed. For this reason one has to be careful to investigate the metabolism of healthy gerbils, a seizure resistant strain is therefore available (Donnelly and Quimby, 2002). Investigating the neuronal metabolism of healthy gerbils is very beneficial for epilepsy research to find differences in metabolism.

1.5 MONITORING NADH AND FAD

For most of experiments shown here, the autofluorescence of nicotinamide dinucleotide hydride (NADH) and flavine adenine dinucleotide (FAD) was

measured. NADH is an important intracellular coenzyme that is involved in various cytosolic and mitochondrial processes. Especially in the energy metabolism of the cell, NADH acts as electron carrier for several core reactions. In the cytosol NAD^+ is reduced to NADH during the glycolysis by Glyceraldehyde 3-phosphate dehydrogenase (GAPDH) and by producing lactate the lactate-dehydrogenase (LDH) NADH is oxidated again. In the mitochondria, the TCA cycle produces NADH, while complex I of the oxidative phosphorylation (OxPhos) is oxidating NADH. In addition the cytosolic NADH can be shuttled over to the mitochondria to fuel the electron transport chain. Moreover, FAD is also an important coenzyme, that acts as electron carrier in the core energy metabolism. In contrast to NADH there are only a few reactions, mainly in the mitochondria, that change FAD levels. In mitochondria it is complex II of the OxPhos, that produces FAD and in the TCA circle FAD is reduced to $FADH_2$ by the Succinic Dehydrogenase (SDH) (Fig. 1.2).

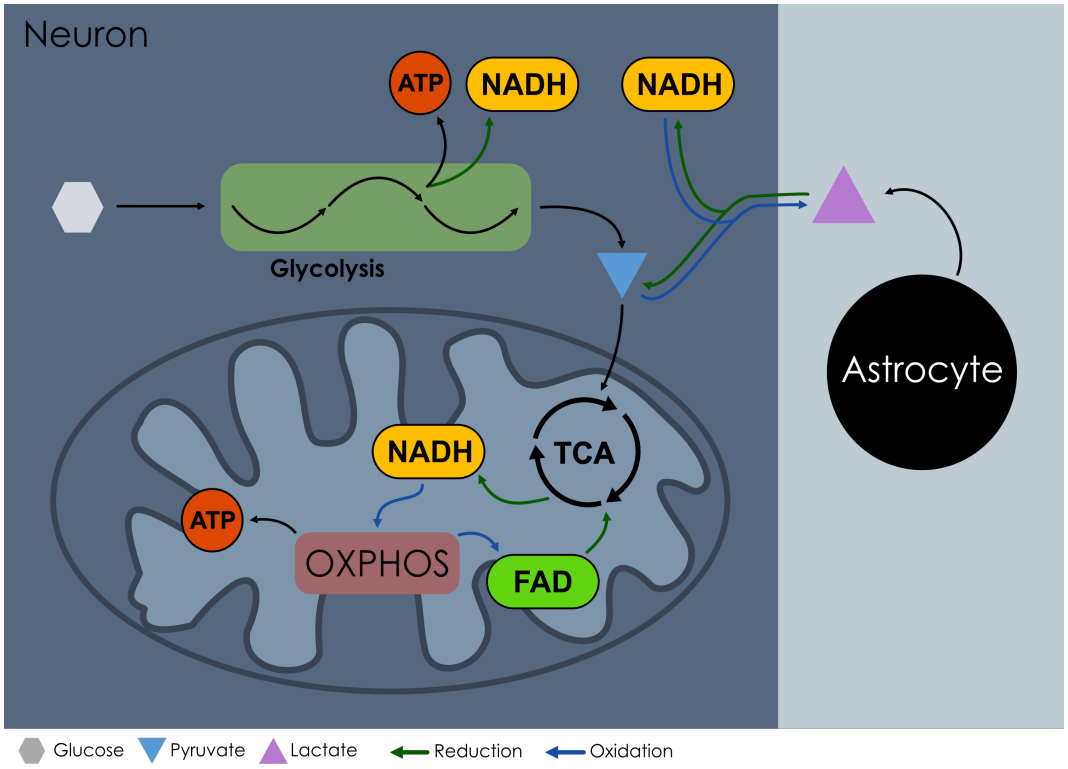

Figure 1.2: Energy Pathways *Schematic of the different energy pathways that produce ATP and use NADH and FAD.*

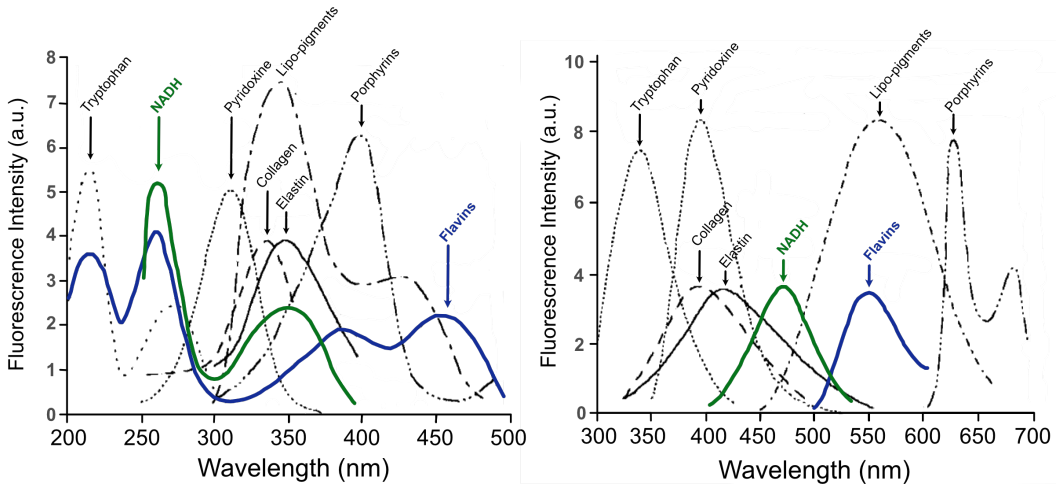

Figure 1.3: Excitation and emission spectra of NADH and FAD *The excitation spectrum of different metabolites and cell elements (left) and emission spectrum (right), In color the two spectra of interest green NADH and blue Flavins. (Adapted from Wagnieres et al. (1998) with permission of John Wiley and Sons - Books. Permission conveyed through Copyright Clearance Center, Inc.)*

In the 50s, Chance et al showed that NADH exhibits autofluorescence in contrast to the oxidised form NAD^+. With this knowledge it was possible to determine the NADH redox state by measuring the fluorescence intensity (Schaefer et al., 2019). Now, NADH autofluorescence intensity can be used as a read out for mitochondrial function. FAD measurements are an even more direct hint of the oxidative metabolism, since cytosolic processes have less influence on the measurements (Shuttleworth, 2010). This was shown by Scholz et al. (1969) where they inhibited the OxPhos with rotenone. This had an influence on both autofluorescence intensities, but after addition of pyruvate NADH signals decreased again while FAD signals showed no significant effect. This effect was explained by the cytosolic autofluorescence of NADH and the LDH turning pyruvate to lactate by oxidating NADH to NAD^+.

Although changes in NADH and FAD give only an indirect hint of the adenosine triphosphate (ATP) production in the mitochondria, it has the advantage that no additional fluorescence dye or biosensor is needed to see changes in metabolite levels.

1.5.1 *Excitation, Emission and Intensity*

The excitation and emission spectra of the two dinucleotides are shown in Fig. 1.3. These spectra can change for some reasons. For example, the emission spectrum of NADH shifts 20-30 nm to a shorter wavelength when it binds to a protein. Depending on the chosen bandpass filter this shift can have an influence on the measured intensity, but such a difference is a manageable problem (Schaefer et al., 2019). Also other proteins or metabolites can change the measured intensity, due to overlapping excitation and emission spectra. For example, collagen increase the total measured intensity, but they should have no influence, in most experiments, on the autofluorescence changes. In contrast, NADPH has the same spectrum as NADH and, under some conditions for example pathological conditions, NADPH levels can change and alter the measured autofluorescence changes. Still, most of the measured changes will originate from NADH, since its level is 10-fold higher and the intensity gets more enhanced in mitochondria (Shuttleworth, 2010). Already early studies showed that the autofluorescence intensity of NADH changes depending on the location in the cell. NADH fluorescence strongly increases in mitochondria and is quenched in the cytosol (Chance and Baltscheffsky, 1958, Shuttleworth, 2010). Therefore, it can be assumed that 90% of the measured autofluorescence origins from the mitochondrial NADH.

1.6 BIOSENSORS

Not all interesting biomolecules in the cell are autofluorescent, for most a sensor is needed in order to determine their levels. For example, for oxygen it is possible to use an electrochemical microelectrode to monitor changes. Forderhase et al. (2020) could even use modified electrochemical electrodes to detect extracellular glucose and lactate levels. Such a microelectrode usually can only determine extracellular levels. Another possibility are biosensors to track specific biomolecules. The first biosensor was built by Clark and Lyons (1962) in order to track glucose concentrations. Nowadays, many different types of biosensors are available, often optical biosensors are used like fluorescent biosensors (Gaviria-Arroyave et al., 2020). These convert the concentration or location of the target molecule into a fluorescence signal. Proteins, small molecules, nucleic acids or lipids can be used as

receptor (Chen et al., 2020). One common technique in the field of neuroenergetics is Förster-Resonance-Energy-Transfer (FRET). Various groups use this genetical encoded biosensor to track different biomolecules of interest. With a genetical encoded FRET-sensor to track lactate concentrations *in-vivo* in neurons and astrocytes, Mächler et al. (2016) found evidence for a lactate gradient from astrocytes to neurons. Another example is Lerchundi et al. (2019), who used an ATP FRET-sensor to track ATP levels.

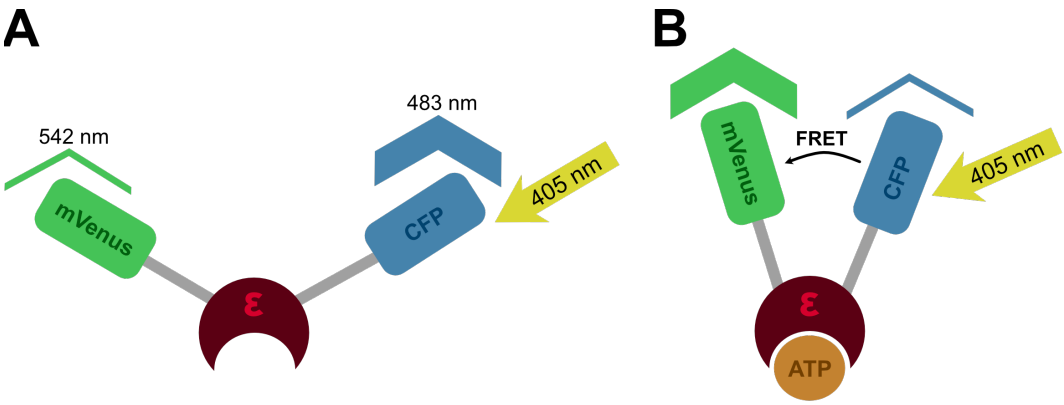

Figure 1.4: *Förster Resonance Energy Transfer principle. (A) no ATP binds to the ε subunit, CFP gets excited but no energy transfer is possible. (B) ATP binds and the conformation changes. CFP and mVenus are close enough for the energy transfer. The emission of mVenus increases while the emission of CFP decreases.*

1.6.1 *FRET-Sensor*

Förster-Resonance-Energy-Transfer (FRET) is a technique that can be used to detect special metabolites like ATP (Fang et al., 2023, Imamura et al., 2009). Such a biosensor has two fluorophores where the emission of the first fluorophor (donor) overlaps with the excitation of the second fluorophor (acceptor). When the two fluorophors are less than 10nm close to each other and the donor gets excited its energy is transmitted to the acceptor and the emission of the acceptor will be visible. To use this energy transfer for metabolite detection the protein has, in addition to the two fluorophores, a binding domain for the metabolite of interest. Without a metabolite at the binding domain, the distance between the fluorophors is to big for the transfer and the emission of the donor will be visible (Fig. 1.4 A). When the right metabolite binds to the domain the conformation of the protein changes and donor and acceptor come close enough together for the energy

transfer (Fig. 1.4 B). By tracking the emission of both fluorophors one can measure changes in metabolite levels.

1.6.2 *Ateam1.03*

Imamura et al. (2009) developed a FRET sensor for real-time tracking of ATP in living cells called ATeam. Their biosensor consists of an ε subunit of a bacterial ATP synthase wrapped by a variant of cyan fluorescent protein (CFP) and monomeric Venus (mVenus), a variant of yellow fluorescent protein (YFP) (Fig. 1.4). The ε subunit has the advantage that it is one of the smallest ATP-binding domains and it binds ATP without hydrolysing it. Additionally, this ε subunit has a remarkably high specificity for ATP, and its conformational change upon ATP binding is significant enough to ensure a broad dynamic range for the FRET signal (Imamura et al. (2009)). The donor fluorophor is a monomeric super enhaced CFP (mseCFP) and as the acceptor are several circulary permuted mVenus, with the 173^{rd} amino acid as its N terminus (cp173-mVenus). This construct is called Ateam1.03 and can detect ATP levels in mM range. Imamura et al. (2009) improved the affinity for ATP even further by changing a few residues, resulting in Ateam1.3^{YEMK}, the version that is used in all experiments explained here.

1.7 MODELLING OF ENERGY METABOLISM

To understand the metabolism of the brain an extremely large number of experiments would be necessary. A computational or mathematical model can help to figure out which hypotheses are more likely than others and to save resources and time to carry out the most valuable experiments. Many different studies are using a theoretical approach aiming for a better interpretation of their experimental data and support of different biochemical or physiological hypotheses. For example, Aubert and Costalat (2005) built a model to test the Lactate Shuttle Hypothesis with classical Michaelis Menten equations and Berndt et al. (2015) has a very complex model that describes the cells in an *in-vitro* situation for a better understanding of NADH autofluorescence measurements. Even though most of these studies validate their models with experiments, two similar models can lead to completely

different interpretations (Somersalo et al., 2012) and vary extremely in their used parameters.

Most studies that investigate a dynamic system achieve this with a mathematical approach of ordinary differential equations (ODE). Such models have the problem of enormous parameter spaces where most parameters can not be determined by experiments (Somersalo et al., 2012). To estimate the missing parameters there are two commonly used methods. One can optimise the model by fitting a curve to the time series of the few measured metabolites. Alternatively, one can deduce them indirectly from measurements of enzyme expression levels or the density of transporters on neuronal membranes. Even though both are valid approaches, both have significant problems (Somersalo et al., 2012). Comparing different models shows how different the parameter space of various models is. Somersalo et al. (2012) addresses these problems by building a probabilistic model, where all incompletely known parameters are modelled as random variables. They encode the lack of information as probability densities.

Another way to build a model is the computational way, for example with a Flux Balance Analysis (FBA). The FBA calculates the flux of various pathways of the metabolism just with a stoichiometry matrix, boundaries for each flux and starting concentrations. It has the advantage that it is a model without any parameters. A drawback of this technique is that it builds on the assumption that the system is minimising or maximising some or several reactions (e.g. ATP production or consumption of glucose and oxygen). Such an assumption is difficult to justify since biological systems are not always optimised (DiNuzzo et al., 2017).

1.8 STUDIES

With the first project, I tried to answer the question: How does the firing frequency impact the use of metabolic pathways in the MNTB? I used NADH and FAD autofluorescence as well as oxygen measurements to determine a difference in the metabolism between lower frequencies and higher frequencies. To identify if a metabolic switch or other adaptations help to sustain the energy demand under various stimulation frequencies, the neurons were electrically stimulated at the fibre tract with frequencies between 10

and 1000Hz. Since the MNTB has such a huge firing frequency range it is a suitable nucleus to investigate the reaction of the metabolism to different firing frequencies. Additional to different frequencies, different stimulation patterns were tested, as well as the impact of the available glucose concentration. Some of these experiments were done in collaboration with Patricia Unterlechner, Cibell Resch, Lukas Voshagen and Valentin Winhart.

My second project tried to extend these studies by measuring ATP directly. This would give further insights in the energy metabolism and it would help to achieve a more accurate model of the system (see Project 3). With a systemic application of an Adeno-associated viral (AAV) vectors via the Vena femoralis, I tried to establish an ATP FRET-sensor in Mongolian gerbils in collaboration with the master student Cibell Resch. So far only in mice and rats an ATP FRET-sensor was established and no systemic application was achieved. A mitochondrial and a cytosolic version of the virus was tested with several expression times in three different brain regions. Finally, the functionality of the biosensor was tested. With this work, I made a first step to achieve ATP measurements in the Mongolian gerbil.

The last project was a completely theoretical approach, where I tested first a DFBA and finally implemented a mathematical steady-state model of the energy pathways of a neuron and an astrocyte. This model should give insights into valuable research directions and help interpreting experimental data. With a sensitivity analysis and a first perturbation of the model with ATP pulses I demonstrate that this model is on a right track.

2

MATERIAL AND METHODS

2.1 ANIMALS

The experiments complied with regional regulations (District Government of Upper Bavaria, 'Regierung von Oberbayern'), national laws (§4 of the German Animal Welfare Act) and with the European Communities Council Directive (2010/63/EU). Mongolian gerbils (*Meriones unguculatus*) of either sex bred in the LMU's certified in-house breeding facility (German Animal Welfare Act, 4.3.2-5682/LMU/Department Biology II) were used for the experiments. Groups of 3 to 4 gerbils were housed with 12 h light/dark cycles at 22.4°C and 66% humidity.

2.2 ACUTE BRAIN SLICES

Mongolian gerbils in the age P30-P40 were anaesthetised with isoflurane (see Drugs) and then decapitated. The brain was removed and transferred to ice-cold slicing solution (see: Solutions). 200 µm thick transverse slices enclosing the MNTB were cut, using a VT1200S Vibratome (Leica Microsystems GmbH, Wetzlar, Germany). Afterwards slices were incubated for 15 minutes at 36°C in carbogen bubbled artificial cerebrospinal fluid (ACSF) (see: Solutions). After this procedure slices were kept at room temperature (23.5°C $\pm$ 1) until they were used for experiments within 5h.

Solutions

Slicing Solution (in mM): 143 sucrose, 25 NaCl, 2.5 KCl, 4 $MgCl_2$, 0.1 $CaCl_2$, 1.25 NaH_2PO_4, 25 $NaHCO_3$, 2 glucose, 3 myo-inositol, 2 pyruvic acid, 0.4 ascorbic acid (Sigma-Aldrich).

ACSF Solution (in mM): 23 sucrose, 125 NaCl, 2.5 KCl, 1 $MgCl_2$, 2 $CaCl_2$, 1.25 NaH_2PO_4, 25 $NaHCO_3$, 2 glucose (Sigma-Aldrich)

Both solutions are finally bubbled with carbogen (95% O_2, 5% CO_2) to ajust the pH to 7.4

2.3 ELECTRICAL STIMULATION

Stimulation was achieved by electrical impulses of a bipolar tungsten electrode (tapered tip concentric microelectrodes, MicroProbes, CEA200). The electrode was placed at the midline (Fig. 2.1A), where the axon fiber bundle of the ipsi and contralateral GBCs crosses and leads to the MNTB neurons. For stimulation of the somatosensory cortex the electrode was placed in the external capsule surrounding the caudate putamen, adjacent to the somatosensory cortex. After the first 15s of recording the stimulation train started, which varied in individual experiments. All stimulations had an amplitude of 5V. The duration ranged from 0.4 to 40s mostly depending on the stimulation frequency, which ranged from 10 to 1000Hz.

2.4 AUTOFLUORESCENCE RECORDINGS

2.4.1 *The setup*

The recordings were performed in a self-designed setup working with light-emitting diodes (LEDs) (for excitation), a camera (for recording) containing a metal–oxide–semiconductor sensor (pco.edge 5.5; PCO AG, Kelheim, Germany) (Direnberger et al., 2015) and a 20X water immersive objective (W Plan-APROCHROMAT, Zeiss, Oberkochen Germany). In the recording chamber slices were superfused with carbogen-aerated ACSF. With pulsed illumination at 365 and 470 nm NADH and FAD were excited, respectively (Huchzermeyer et al., 2008, Shuttleworth, 2010, Brosel et al., 2018, Schaefer

et al., 2019). To track only the interesting wavelengths a multiband filter was used for excitation (AHF F69-390) and emission (AHF F72-622). NADH and FAD fluorescence images were recorded alternating at a frequency of 4 Hz with an acquisition time of 20ms. In total, the autofluorescence was recorded for 90 seconds.

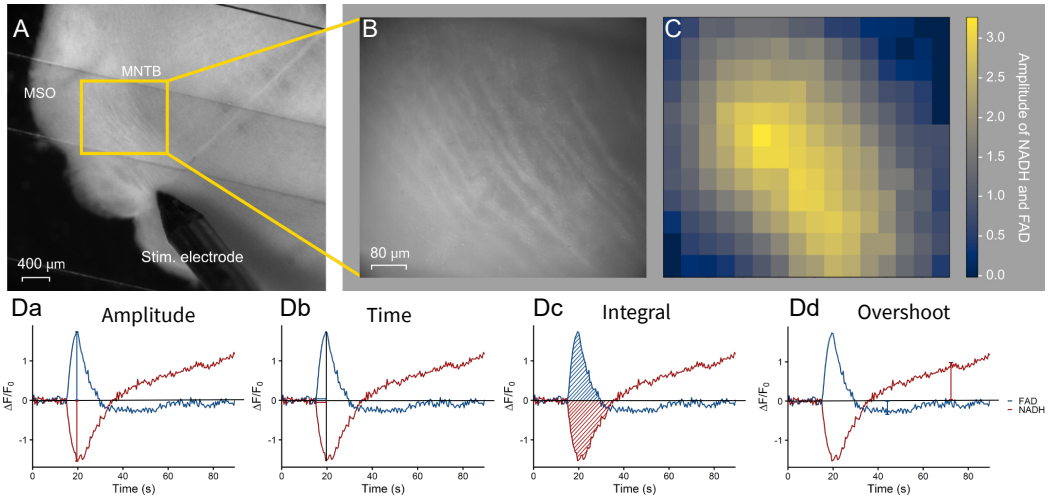

Figure 2.1: Brain slice and measured parameters *(A) An acute brainstem slice with SOC nuclei, the bipolar stimulation electrode is placed at the midline where the fibers of the contra- and ipsy-lateral GBCs are crossing, 5 × magnification. (B) 20 × magnification of the MNTB. Within this region autofluorescence is measured. (C) Heatmap that shows the sum of NADH and FAD amplitudes for every ROI. For further analysis the ROI with highest sum was chosen. (D) Different parameters that can be calculated from the time series: (Da) the amplitude of the peaks, (Db) the time from stimulation start until the peak, (Dc) the area under the curve, the integral, (Dd) the overshoot. Adapted from Palandt et al. (2023).*

2.4.2 *Preprocessing and Analysis*

With the described setup one can capture autofluorescence signals of the entire nucleus. For further analysis, I implemented a python script (Python 3.9.12) to identify the region with the highest sum of NADH and FAD peak amplitudes. For this purpose the script divided every image into 192 (16 x 12) rectangular regions of interest (ROI) with a size of approximately 50µm x 50µm (Fig. 2.1). The ROI that mostly showed the highest sum in different experiments of a session, was chosen for analysis of every experiment on the same brain slice.

A linear function was fit through the data points of the first 15s to correct the bleaching of the autofluorescence data. I present the fluorescence signals here as $\Delta F/F_0$. Where ΔF is the difference between the total fluorescence and bleaching fit, and F_0 is the fluorescence at the beginning of the recording. As described above a multiband filter was used to monitor NADH and FAD in the same experiment. The excitation spectrum (Fig. 1.3) reveals that in this setup FAD got excited at 360nm as well and a bleed-through of FAD in the NADH images occurred. This bleed-through was corrected by subtracting a calculated FAD autofluorescence from the NADH autofluorescence image. More details can be found here: 4.6.5 Appendix.

From this preprocessing arise two time courses, that were used for analysis. Many parameters can be calculated that can be compared between experiments (Fig. 2.1D). The most interesting ones are the amplitudes of the extrema, the time from stimulation start until the extrema is reached, the integral of the curves between stimulation start and the overshoot of the time course (Brosel et al., 2018).

2.5 O_2 MEASUREMENTS

Recording of extracellular O_2 was done with an electrochemical O_2 microelectrode with a 10µm-diameter tip (Unisense A/S, Aarhus, Denmark) (Huchzermeyer et al., 2013, Brosel et al., 2018). For calibration 3 points with known O_2 level were measured: 0% (0.1M ascorbic acid and 0.1M NaOH), 20% (air-bubbled ACSF) and 95% (carbogen-bubbled ACSF). The tip of the electrode was placed just under the surface of the tissue, within the region of interest.

2.6 PHARMACOLOGY

Complex I, III and IV of the OxPhos were blocked with 10 µM rotenone (Sigma-Aldich; cat.No. 45656 (year 2019); stock solution 5mM in ethanol), 10 µM antimycin A (Sigma-Aldrich; Cat.No. A8674 (year 2019); stock solution 90mM in ethanol) and 10 µM potassium cyanide (Sigma-Aldrich; stock solution 10 mM in H_2O). In all experiments that included these blockers they were added to the ACSF and from that point on every 5min the change

in autofluorescence signals upon stimulation was measured. After 20 min of blocking the blockers were washed out with normal ACSF.

2.7 ATP FRET SENSOR

2.7.1 *The Virus*

Adeno-associated viral (AAV) vectors with AAV2 as backbone and AAV-PHP.eB as capsid were used to transduce neurons. AAV-PHP.eB is known to cross the BBB and enter cells in the central nervous system (Chan et al., 2017, Hordeaux et al., 2019). To assure that only neurons express the virus, human synapsin 1 as a neuron-specific promoter was used (Fig. 2.2). A second virus was used with an additional mitochondrial-specific promoter for an expression only in the mitochondria of neurons. With those two viruses, it is possible to compare the ATP changes in the cytosol with those in the mitochondria. The plasmids contained an open-reading frame of the ATP sensor ATeam1.03$^{\text{YEMK}}$ (see Imamura et al. (2009)). All viruses for the experiments here were made by Dr. Chu Lan Lao, (LMU; BMC; Prof. Götz).

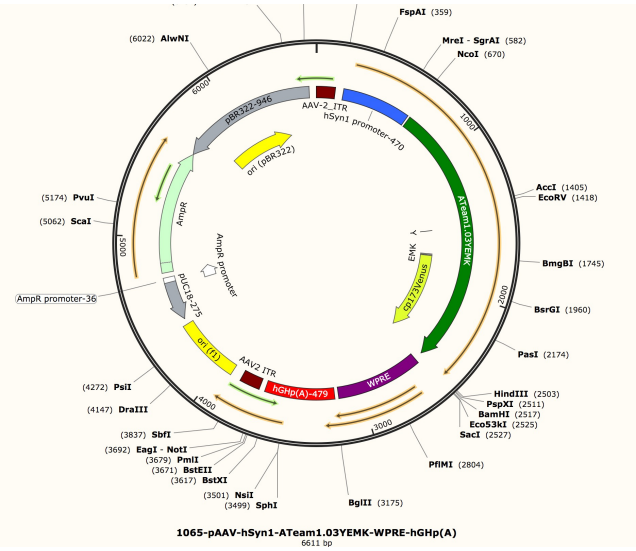

Figure 2.2: *Plasmid map of the cytosolic virus*

In the literature a systemic application of AAV-PHP.eB needs an expression time between 3 and 4 weeks and a sufficiently high concentration is neces-

sary (Dayton et al., 2018). Here different expression times were compared from 3-5 weeks.

2.7.2 *The injection and slice preperation*

All injections were conducted under Tierversuchantrag Nr.: ROB-55.2-2532.Vet_02-19-147 (Regierung von Oberbayern). For the systemic application of the virus, Mongolian Gerbils in the age around P30 were initially anesthetised with isoflurane. Afterwards, adjusted to the body weight, the animals were anesthetised with MMF (see Drugs). Once the anaesthesia became effective, the gerbil received an oxygen supply and was placed on a heated plate to maintain a stable body temperature. To prevent dryness, eye ointment (Bepanten) was applied to cover the eyes. As described in Pérez-Garcõ et al. (2003) the inner side of one thigh of the animal was shaved and after applying a small cut in the skin in parallel to the blood vessel, the virus suspension was injected into the Vena femoralis. After the injection the skin gets sewn with one stitch and iodine is used for disinfection. Afterwards buprenorphine as pain killer was injected intraperitoneal followed by antagonisation of anaesthesia using AFN (see Drugs), according to the body weight. Then the gerbil was laid under infrared light and it was placed under surveillance until it woke up. For the following week the animals were monitored every day and later once a week.

Drugs	
Isoflurane	IsoFlo®, 100% isoflurane; Zoetis Schweiz GmbH
MMF	5 mg/kg Midazolam (Braun GmbH; 5 mg/ml) 0.5 mg/kg Medetomidine (Oreon Pharma; Domitor 1 mg/ml) 0.05 mg/kg Fentanyl (Jannsen Pharmaceutica; 0.05 mg/ml)
Bepanthen	Bayer AG; active reagent 5 % Dexpanthenol
Buprenorphine	Bayer AG; Buprenorvet 0.3 mg/ml
AFN	2.5 mg/kg Atipamezol (CP Pharma; Revertor 5 mg/ml) 0.5 mg/kg Flumazenil (Hexal AG; 0.5 mg/ml) Naloxon

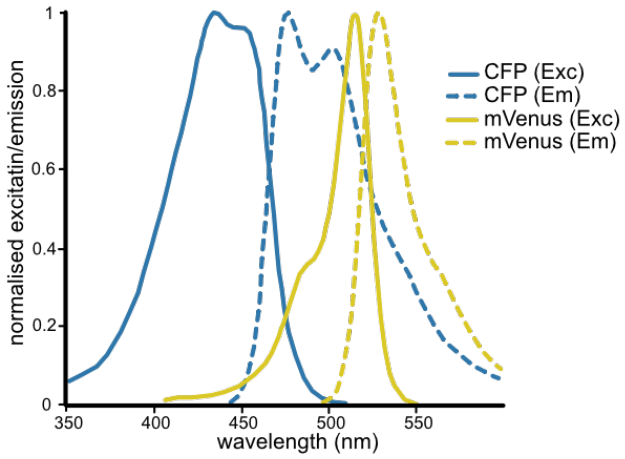

Figure 2.3: Spectrum of ATeam1.03^{YEMK} *Excitation and emission specrta of the two fluophores of the FRET-sensor.*

After different expression times between 1-5 weeks, the animals were anesthetised with isoflurane and decapitated. The brainstem and the cortex were cut into 200µm or 300µm thick slices as explained in 1.6.2 Acute Brain Slices.

2.7.3 *The Setup*

A 405nm LED excited the FRET sensor to measure its fluorescence emission. The emission fluorescence was split at 500nm in an image splitter (Hamamatsu Photonics Deutschland, Hersching, Germany) with a beam splitter FF509-FDi01 (Semrock, West Henrietta, NY,USA). It reflects lower wavelengths and transmits higher ones, which are then filtered with a bandpass filter at 483/32 (CFP) and 542/27 (mVenus; both Semrock). The Venus channel shows the level of ATP bound biosensors and the eCFP channel showed the level of ATP-free sensors (Fig. 1.4), the ratio of those two channels is used as measurement of the ATP levels in the cells. Images were recorded every second for 180 seconds in total.

Analysis of FRET channel images

With the beam splitter two fluorescence wavelengths were recorded at the same time. Both images were divided into 72 (6×12) ROIs and performed

the analysis for one ROI. To correct the bleaching the following formula was fitted to the first 30 images and the last 20 images:

$$y = a * e^{-bx} + c * e^{gx} + h$$

with a,b,c,d,g and h as variables to fit. After the bleaching correction the fluorescence change ($\%\Delta F/F_0$) was calculated for each time point.

2.7.4 *Immunohistochemistry*

To detect, whether the virus was expressed in neurons, the brain slices were postfixed in 4% paraformaldehyde (PFA) overnight. To compare different brain regions that were not sliced, the remaining brain was postfixed as well. The 200µm thick brain sliced were stained free-floating in a 12-well plate. First they were incubated in blocking solution (1.5% Triton X100, 1% BSA, 0.1% Saponin in PBS) for 30min. For other brain regions the brain was washed 3 times in PBS for 10 min and afterward cut into 60µm slices with a Vibratome (Leica VT1200S, Wetzlar, Germany). These coronal slices were placed on Superfrost Plus Adhesion Microscope Slides coverslips (J1800AMNZ, Epredia, Portsmouth, NH, USA), then the application of antibodies could commence within a wet chamber. First the slices were incubated for 2 days at 4°C with the primary antibody recombinant GFP protein that binds to mVenus, which is part of the FRET sensor. As secondary antibody A488 and Nissl-b 435/455 were incubated overnight at 4°C. The free floating slices were then placed on coverslips and mounted in Vectashield medium (H-1000, Vector Laboratories, Burlingame, CA, USA). With a Nikon Eclipse 80i and a 20X objective (Plan Fluor, Nikon, Tokyo, Japan) images of the stained brain slices were taken.

2.7.5 *Test of functionality*

To test if ATP changes are detectable in the slices, that express ATeam1.03^{YEMK}, two different methods were used. First, the slices were stimulated with 400 pulses at 10Hz. To achieve this in the somatosensory cortex a bipolar tungsten electrode (tapered tip concentric microelectrodes, MicroProbes, CEA200) was placed in the external capsule surrounding the caudate putamen, adjacent to the somatosensory cortex.

In the second method, the intracellular ATP concentration was increased. As described in the protocol of Lerchundi et al. (2020) the neurons were first permeabilised with 30 µM escin (Sigma Aldich, Saint Louis, MO, USA) in carbogen-bubbled ACSF for 30 min. Then the slice was put into the recording chamber. After 30s of recording, 1mL of 20mM ATP was pumped to the recording chamber. Afterwards the pump was turned off leaving 2mL ACSF with 10mM ATP in the recording chamber. Changes in ATeam1.03^{YEMK} fluorescence channels were monitored.

2.8 THE MODEL

I used two methods to implement the model, a computational approach for a dynamic flux balance analysis (DFBA) and a classical mathematical approach. The DFBA was done using MATLAB R 2021b (The MathWorks Inc. (2021)) and the toolbox of Dromms et al. (2020). For implementing the mathematical model and steady-state analysis the IQM Toolbox from IntiQuan was used working on MATLAB R 2020a (The MathWorks Inc. (2021)).

2.8.1 *Dynamic Flux Balance Analysis*

In a FBA the biochemical network is presented by a stoichiometry matrix $S(m \times n)$, with n columns of reactions and m rows of metabolites. It calculates the fluxes $\vec{v}$ through this network of reactions. A normal FBA assumes that the system is in steady state (Orth et al., 2010). This assumption allows to calculate the fluxes as follows:

$$S\vec{v} = 0$$

Such a linear equation system has many possible solutions. For this reason, the number of possible solutions are reduced by setting a range in which each flux is allowed to be.

$$\vec{v}_{LB} \leqslant \vec{v} \leqslant \vec{v}_{UB}$$

With these constraints an allowed solution space is defined, that probably still contains many possible solutions. To decide for one solution one or several reactions are optimised, e.g. maximising growth rate of the organism or the ATP production. With this setup a solution is found that maximises or minimises the flux of the chosen reactions (Orth et al., 2010). Such a method does not need any kinetic parameters, that are often difficult to measure or even unknown. Further, it allows a very fast computation and with it, it is possible to use genome scale metabolic networks. But for tracking of metabolite concentrations and perturbation of the system this basic method is not sufficient, since one can only model a system in steady state. For this reason a DFBA is necessary. There are two main DFBA approaches the static optimisation approach (SOA) and the dynamic optimisation approach (DOA) (Scott et al., 2018). With the SOA the extracellular fluxes can change dynamically, and it stays a linear programming problem. In contrast, the DOA has time profiles of fluxes and metabolites, which leads to a non-linear programming problem and makes it difficult to solve it for huge metabolic networks (Mahadevan et al., 2002). The SOA is not sufficient for dynamic systems as neurons and the DOA needs long computation times. Finally, a third option occurred that solved these problems. Recently a new approach was published inventing a linear kinetics dynamic flux balance analysis (LK-DFBA) (Dromms et al., 2020). They introduced pooling fluxes, for every metabolite, that were added to the normal stoichiometry matrix. This allows to track the metabolite concentrations and gives the possibility to optimise metabolite concentrations.

$$A\vec{w} = \begin{bmatrix} SP \end{bmatrix} \begin{bmatrix} \vec{v} \\ \vec{v}_p \end{bmatrix} = 0$$

where A is the augmented stoichiometry matrix $(m \times (n + m))$ and $\vec{w}$ is the augmented flux vector $((m + n) \times 1)$.

The second new advantage of the LK-DFBA is that it adds linear kinetics as additional constraints that reduce the number of possible solutions and reduce the possibility of biologic irrelevant solutions. With this way one can add every kind of positive or negative regulation, that can be expressed in a linear function.

2.8.2 *Mathematical Approach*

To achieve a steady state, a mathematical model of ordinary differential equations (ODE) was built to estimate steady-state fluxes and steady-state concentrations. The mathematical model for a specific reaction can be determined by the enzyme and its expression levels (Somersalo et al., 2012). The most simple approach is to use the classic Michaelis-Menten kinetic. With this, the flux v of reaction R1 that transforms substrate A to product B can be calculated.

$$\begin{gathered} R1 : A \rightarrow B \\ v = V_{max} \times \frac{[A]}{K_m + [A]} \end{gathered} \tag{2.1}$$

with the concentration of species A $[A]$, V_{max} as maximal reaction velocity and the Michealis constant K_m. If a reaction R2 needs more than one substrate or additional a cofactor the Michaelis-Menten kinetic changes as follows:

$$\begin{gathered} R2 : A + B \rightarrow C \\ v = V_{max} \times \frac{[A]}{K_m^A + [A]} \times \frac{[B]}{K_m^B + [B]} \end{gathered} \tag{2.2}$$

Also, the inhibition of enzymes can be modelled by a form of the classic kinetic. In this model mostly noncompetitive inhibitions were included like product inhibition where Reaction R3 gets inhibited by product B:

$$\begin{gathered} R3 : A \rightarrow B \\ v = V_{max} \times \frac{[A]}{[A] + K_m \left(1 + \frac{[B]}{K_i}\right)} \end{gathered} \tag{2.3}$$

where K_i is the dissociation constant.
The transport between compartments can be passive diffusion for gases as

O_2, since no enzymes are involved in such a transport the flux depends on the diffusion coefficient λ:

$$v = \lambda([A]_{c1} - [A]_{c2}) \tag{2.4}$$

where $[A]_{c1}$ is the concentration of A in compartment 1 and $[A]_{c2}$ the concentration in compartment 2. When carriers are involved in the transport a similar kinetic can be used as for enzymatic reactions (see Eq. 2.1), with the affinity a instead of K_m and the maximal transport rate T_{max} for V_{max}. An isotropically carrier function can be modelled by:

$$v = T_{max} \times \left(\frac{[A]_{c1}}{a + [A]_{c1}} - \frac{[A]_{c2}}{a + [A]_{c2}} \right) \tag{2.5}$$

With these 5 kinetics all reactions in the model were described. The detailed reactions with the used parameters can be found in the Appendix.

Compartments

Most brain energy metabolism models have multiple compartments. This system was also divided into four compartments: the extracellular space (E), the astrocyte (A) and the neuron with cytoplasm (NC) and mitochondria (NM) (Fig. 2.4). The differentiation between cytosol and mitochondria in Neurons is mainly important to distinguish between cytosolic and mitochondrial NADH. There is no difference between mitochondria and cytosol in astrocytes because their mitochondria were modelled as a black box.

Irreversible model

Many reactions in the glycolysis or the TCA cycle are reversible reactions. To avoid random fluxes that keep the steady state for false reasons, almost all reactions are modelled irreversible. In the glycolysis the reactions flow toward pyruvate, in the TCA cycle the reactions flow toward oxalacetate. The lactate-shuttle is the only reaction that was kept reversible since the direction of the flow of lactate can change depending on the ATP consumption of the neuron (Fig. 2.4).

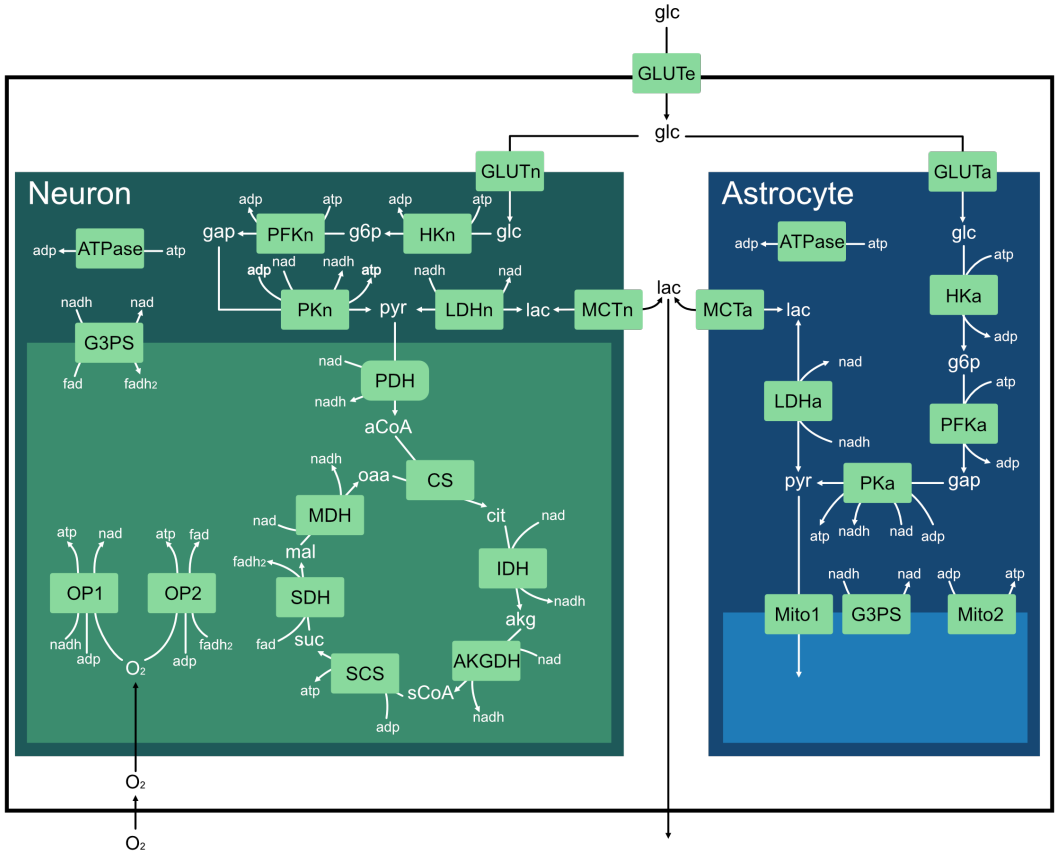

Figure 2.4: Model Pathways. *All pathways implemented in the model, are divided in 4 compartments: Extracellular Space, Neuron Cytosol, Neuron Mitochondrion, and Astrocyte. The following pathways are included: Glucose Transporters, O_2 Diffusion, Glycolysis, Lactate Shuttle, TCA, OxPhos (OP1 and OP2); more details are found in the Appendix. Colour code: Green background: Neuron, Blue background: Astrocyte; dark colour: Cytosol, light colour: mitochondria. An explanation of all the abbreviations can be found in the List of Abbreviations.*

A steady-state model

In order to achieve a steady state several simplifications of the system were performed. The number of reactions were reduced to get a simple model, where only necessary reactions are included. This has the advantage that it reduces the number of parameters drastically. It is possible to increase the complexity of the model later when certain reactions appear to be of interest. The needed parameters V_{max}, K_m and K_i are adapted from Berndt (2012), Berndt et al. (2015) or Genc et al. (2011). With the kinetics and parameters

found in the Appendix, a model was built that could achieve a steady state over some time. The starting concentrations were then set to these steady state concentrations.

Analysis

With a sensitivity analysis, it is possible to determine the parameters that are especially sensitive to the system. From this analysis one can locate the subsystem that is more rate-limiting than others and is worth a more detailed analysis.

To make a first proof-of-principle the model was perturbed after 15s (as in the *in-vitro* experiments) with an ATP pulse that simulates the ATP consumption during neuronal activity.

2.9 STATISTICAL ANALYSIS

For statistical analysis R (version 4.2.1, R Core Team (2022)) was used. All presented data shows the mean ±SEM (standard error of mean). Normal distribution was tested for all data sets with a Shapiro-Wilk test and an additional graphical analysis with a Q-Q plot. To test the statistical significance depending on the question different tests were used: linear regression, a two-sided t-test or a paired t-test with Bonferroni correction. An overview of the p-values of the different tests can be found in Appendix: P-Values

3

RESULTS

3.1 AUTOFLUORESCENCE STUDY

The following section describes the same results that are presented in Palandt et al. (2023).

3.1.1 *Frequency Dependence*

How much is the metabolic readout in the MNTB dependent on the stimulation frequency? To answer this question the neurons were stimulated for 5s with different frequencies ranging from 10 to 1000 Hz. This first approach is similar to the experiments in the LSO of Brosel et al. (2018). Also the results showed a similar outcome, the amplitudes of NADH and FAD increase until they reach a plateau (Fig. 3.1Ab). These increasing amplitudes can be explained since with increasing frequency the number of action potentials (APs) increases and with it the amount of needed ATP.

For this reason, a second experiment was carried out. This time the cells were triggered with 400 stimuli at frequencies ranging from 10 to 1000Hz (Fig. 3.1Ba). The amplitudes of the peaks show now a different result, again they increase up to 100Hz and after that both amplitudes decrease for increasing frequencies (Fig 3.1Bb). The time to the peak is decreasing with the increase in frequency (Fig. 3.1). The integral of the curves was as well decreasing with increasing frequencies (Fig. 3.1Bd). This shows that even though the peak amplitude of the two dinucleotides increase from 10 to 100Hz the integral is already quite big for these lower frequencies. For a

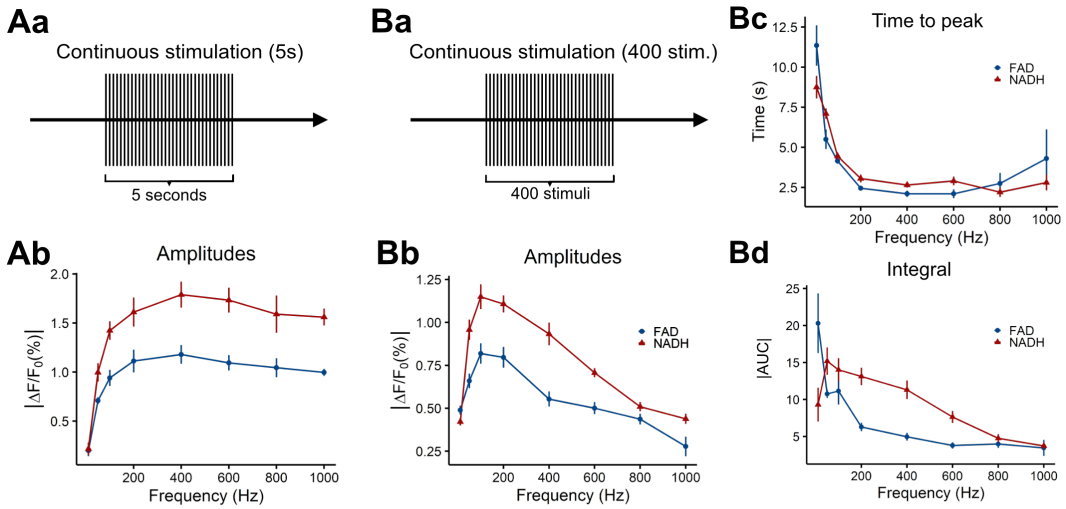

C

freq. (Hz)	10	50	100	200	400	600	800	1000
#stim.(A)	50	250	500	1000	2000	3000	4000	5000
time(s) (B)	40	8	4	2	1	0.6	0.5	0.4

Figure 3.1: Frequency dependence of NADH and FAD amplitudes for different stimulation patterns *(A) Continuous stimulation for 5s (Aa) and the resulting changes for NADH and FAD peak amplitudes (see Fig. 2.1Da) origins by oxidation of NADH and $FADH_2$ (the first phase of the autofluorescence response) (Ab). (B) The amplitudes of the NADH and FAD signals (origins by maximal oxidation of NADH and $FADH_2$) (Bb) while stimulating the fibres with different frequencies for varying duration to apply always 400 stimuli (Ba). (Bc, Bd) Changes in time to peak (time between start of stimulation and extrema) (Bc; for analysis see Fig. 2.1Db) and integral under the curve (Bd; for analysis see Fig. 2.1Dc) for alteration of NADH and FAD levels after 400 stimuli at different frequencies. (C) Comparison of total number of stimuli for 5-s stimulation (A) and of stimulation duration for experiments applying a fixed number of 400 stimuli (B). Data points represent mean +/-SEM; A: n = 9, N = 5; B: n = 10, N = 5; n = #stimulations; N = #animals. Figure and caption adapted from Palandt et al. (2023).*

more detailed analysis the O_2 consumption during these experiments were evaluated.

3.1.2 *O_2 consumption*

The experiments with fixed number of stimuli (stimulation protocol: Fig. 3.1Ba) were combined with extracellular O_2 measurements. Typical O_2

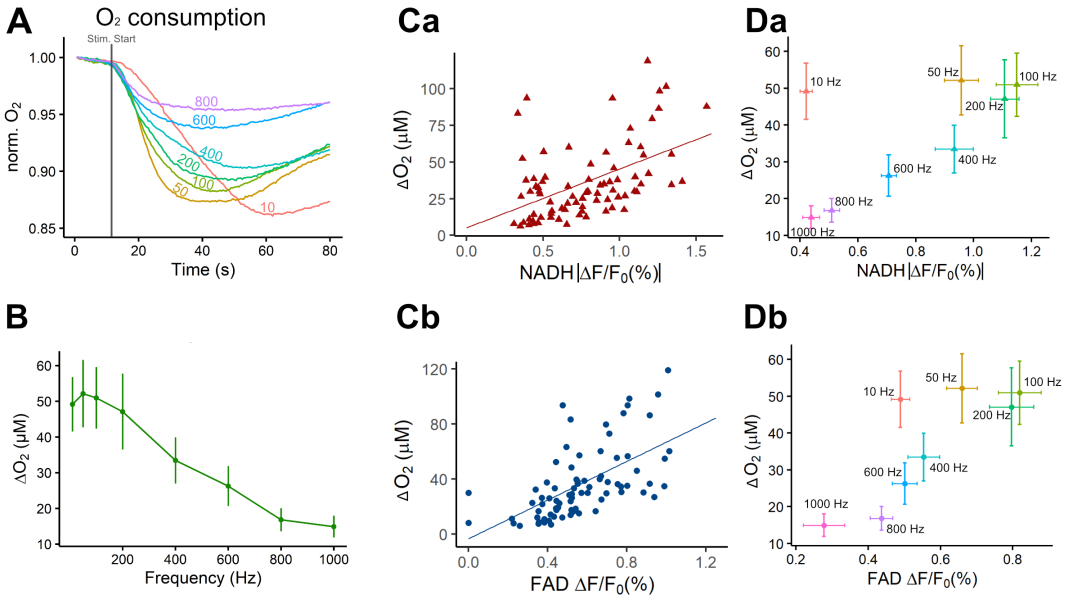

Figure 3.2: O_2 consumption due to stimulation with 400 stimuli at different frequencies *(A) Example of time course of the normalised O_2 concentration after stimulation with different frequencies. (B) O_2 consumption for varying stimulation frequencies. (C) Correlation between O_2 consumption and NADH (p-value = 4e-6, R^2 = 0.23) (Ca) and FAD amplitudes (p-value = 5.29e-9, R^2 = 0.35) (Cb). (D) Mean amplitudes and SEM of O_2 consumption as function of NADH (Da) and FAD amplitudes (Db) at different frequencies. Data points represent mean +/-SEM; n = 10, N = 5; n = #stimulations; N = #animals. Figure and caption adapted from Palandt et al. (2023).*

curves for different stimulation frequencies are shown in 3.2A. From this it can be suggested that the amplitude of the O_2 consumption decreases with increasing frequency. Fig. 3.2B reveals that the mean O_2 consumption stays similar from 10 to 200Hz and then decreases with increasing frequency. These observations fit mostly to the autofluorescence measurements, a linear regression reveals that the NADH and the FAD amplitude is correlated with the O_2 amplitude (Fig. 3.2C). Only for the frequencies 10 and 50Hz the O_2 amplitude is high and constant while the autofluorescence amplitudes increase (Fig. 3.2D). These observations lead to the suggestion that the OxPhos is an important pathway especially for low frequencies, while higher frequencies rely more on different energy pathways.

3.1.3 *Block of OxPhos*

The O_2 consumption during low frequency stimulation shows the importance of the OxPhos. To support this assertion complexes I, III and IV of the OxPhos were blocked and the cells were stimulated with a frequency of 50Hz. Comparing the amplitudes of NADH and FAD signals, revealed a significant decrease of both amplitudes. This partially recovered after the washout of the blockers (Fig. 3.3). This confirms the importance of OxPhos for low firing frequencies.

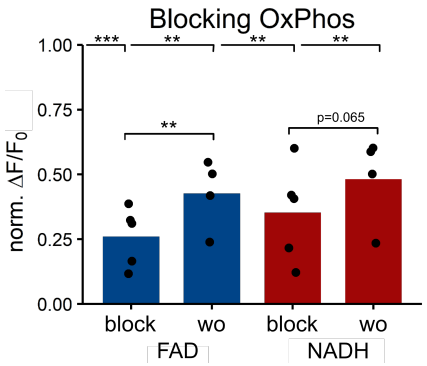

Figure 3.3: Blocking of OxPhos *NADH and FAD amplitudes normalised to the respective control values after 400 stimuli with 50Hz. The measurements were done while blocking OxPhos with rotenone, antimycin A and potassium cyanide (10µM each; block) and after washout (wo). Points represent individual experiments and the bars mean values at 50 Hz stimulation. All values are significantly different from 1, i.e. the unblocked control condition as tested by one-sample t test (* $p < 0.05$, ** $p < 0.01$, *** $p < 0.001$). For FAD, washout was significantly different from blocking (paired t-test, p value = 0.0070), for NADH it showed a tendency (p value = 0.0654). #slices n = 5. Figure and caption adapted from Palandt et al. (2023).*

3.1.4 *Burst mode*

A continuous stimulation is not a physiological firing pattern for all neurons. Especially neurons that are capable of high-frequency firing often show a bursting activity pattern. Additionally, it was shown that in thalamocortical neurons the average firing rate determines the metabolic costs (Yi and Grill, 2019). To mimic this more physiological condition, the cells were stimulated with 400 impulses over a period of 5s. To achieve this for all frequencies

the 400 stimuli were divided in 80 bursts, a burst contains 5 impulses in the respective stimulation frequency, between two bursts is a varying break depending on the frequency (Fig. 3.4A). Frequencies below 100 Hz were not applied, because a longer stimulation period than 5s would have been necessary to apply 400 impulses.

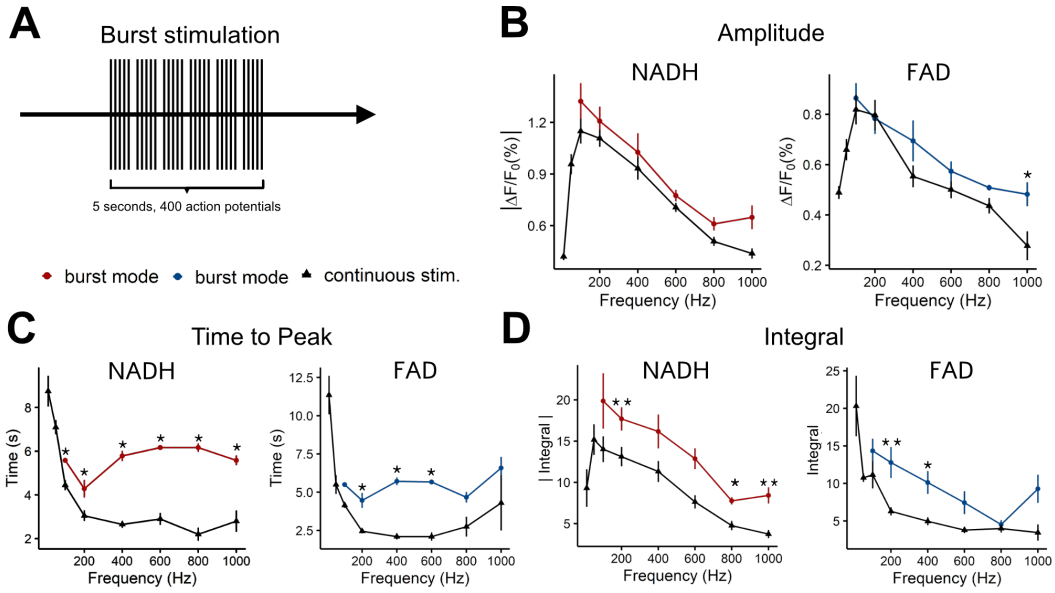

Figure 3.4: Stimulation in burst mode *(A) The stimulation pattern of the burst mode. Comparison of different parameters after 400 continuous and burst stimuli. (B) Amplitudes of NADH and FAD, (C) time to peak of NADH and FAD, (D) integral of NADH and FAD signals. Represented is the mean ± SEM. # stimulations n: burst mode: n=7 (600, 800 Hz n=3); continuous stim.: n=10. Significance: (B,D) * $p < 0.05$, ** $p < 0.01$, *** $p < 0.001$; (C) * $p < 0.01$ Adapted from Palandt et al. (2023).*

Comparing the amplitudes of NADH or FAD for the two stimulation patterns no significant difference was found (Fig. 3.4B), only the amplitudes at 1000Hz are significantly different (two-sided t-test: p-values: FAD: 0.024; NADH: 0.055). The integral after stimulation in burst mode is significantly larger for half of the frequencies of NADH and FAD curves (More details about the p-values can be found in Tab. 1). The trend remains consistent as higher frequencies correspond to a decrease in the integral. (Fig. 3.4D). A possible reason for these observations of significantly higher amplitudes and integrals could be that the breaks between the bursts help the neurons to recover better, and the actual firing rate is closer to the stimulation rate. The time to the peak is significantly longer. Instead of decreasing as for

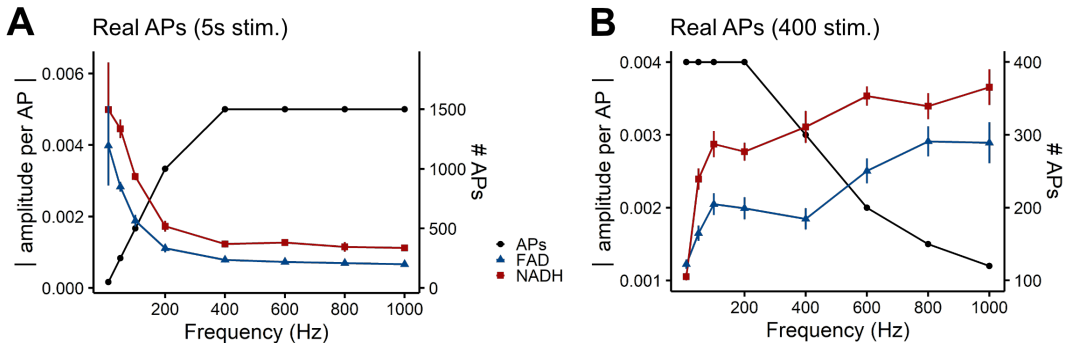

Figure 3.5: Peak amplitudes per AP *Amplitudes of changes in NADH and FAD levels per individual AP for a fixed stimulation duration of 5 s (A) and for a fixed number of 400 APs (B). Values considering the real number of APs in MNTB principal cells based on the literature. Data points represent mean +/-SEM; A,C: n = 9; B,D: n = 10; n = #stimulations. Figure and caption adapted from Palandt et al. (2023)*

continuous stimulation the time to the peak is constant around 5 to 6s for both NADH and FAD (Fig. 3.4C).

3.1.5 *Amplitude per AP*

For frequencies above 200 Hz it is not possible to distinguish if the amplitudes are decreasing due to a metabolic switch or a reduction in the actual firing rate due to a reduced reliability of the principal neurons at high frequencies (Kopp-Scheinpflug et al., 2003). Based on *in-vivo* measurements (Taschenberger and Von Gersdorff, 2000, Kopp-Scheinpflug et al., 2003, 2011, Borst and Soria Van Hoeve, 2012) and cell-attached *in-vitro* recordings (Grande and Wang, 2011) a simple estimation of the actual firing rate was done, stimulation frequencies below 300 Hz were assumed to be equal to the firing rate. For stimulation above 300 Hz failures occur and, therefore, an average firing of 300 APs per second is assumed. According to the estimated firing rate the amplitude per AP was calculated (Fig. 3.5). For the experiments with a fixed stimulation duration, the amplitude per AP decreases for increasing frequencies until it reaches a plateau at 200 Hz (Fig. 3.5A). This result supports the idea of a metabolic switch for higher frequencies toward glycolysis.

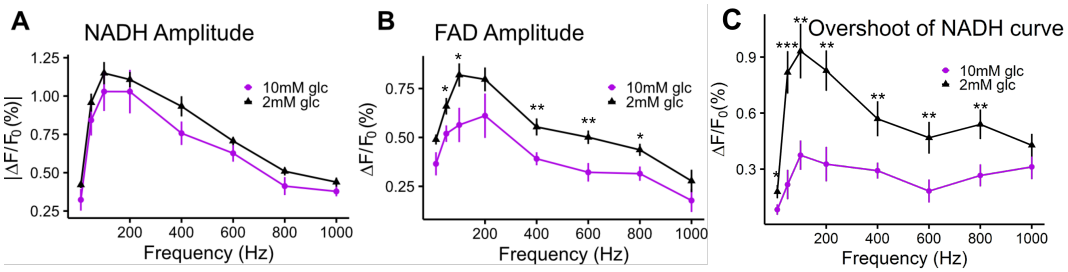

Figure 3.6: Influence of different glucose concentrations *Changes of different parameters due to different glucose concentrations in the ACSF after 400 stimuli at different frequencies. (A, B) Amplitudes of NADH (A) and FAD (B) for a glucose concentration of 2 mM (same data as shown in Fig 3.1) and 10 mM. (C) Overshoot of the NADH time course. Data points represent mean +/-SEM; n = 10 (2mM glc), n = 9 (10mM glc); n = #stimulations. Significance: * p < 0.05, ** p < 0.01, *** p < 0.001. Figure and caption adapted from Palandt et al. (2023)*

Further insights give the experiments with 400 stimuli. For frequencies, up to 100 Hz the amplitude per AP increases, this is in contrast to the data with fixed stimulation of 5s (Fig. 3.5). For higher frequencies, the amplitude per AP does not increase much further, but it is 3 times larger than the amplitudes per AP during a 5s stimulation. Overall the amplitude per AP is lower when more APs are triggered. This could be explained by an increasing ATP consumption of a single AP the fewer APs in total are triggered. Another possibility is the a metabolic switch depending on the number of triggered APs.

3.1.6 *Impact of glucose concentration*

The concentration of glucose in the ACSF has an impact on the metabolical pathways that the cells can use. Here the glucose concentration was enhanced from 2mM to 10mM, to see the impact on NADH and FAD autofluorescence. A glucose concentration of 10 mM matches the conditions in most *in vitro* experiments. The cells were stimulated with 400 electrical impulses at different frequencies.

As expected, the FAD amplitudes are significantly lower with the higher glucose concentration. This can be explained by a shift towards the glycolysis (Fig. 3.6B). Interestingly, the NADH amplitudes were not significantly

different (Fig. 3.6A). A possible explanation is that a lot of pyruvate is produced, which feeds the LDH to produce lactate. Since the LDH oxidises NADH, this cytosolic reaction might increase the amplitude slightly. Other parameters show no interesting change except for the overshoot of the NADH curve. Here the overshoot decreases drastically for all frequencies except 1000 Hz (Fig. 3.6C) (the exact p-values can be found here: Tab. 3), which indicates a shorter second phase.

3.2 ATP FRET SENSOR

3.2.1 *Expression of the virus*

The first experimental step was to figure out how long the expression time has to be. Expression times between 1 and 5 weeks were compared. For better visualisation, the cells were stained with a Nissel and a GFP antibody, that binds to mVenus. In the first two weeks, there was no expression visible in the brainstem. With the mitochondrial Ateam1.3^{YEMK} in the third week, some cells expressing the virus were visible in the cortex and the hippocampus (Fig. 3.7). It seems to be an all-or-nothing expression since all cells show a high expression or no expression at all. In the 4^{th} and 5^{th} week the number of positive cells in the cortex and hippocampus seem to increase. However, counting showed no significant increase in the number of positive cells (Fig. 3.8). Interestingly, all positive cells were found at big arterioles. In the SOC the longer expression time did not help, only in the 5^{th} week a single cell expressing the virus was found (Fig. 3.7).

To improve expression a less specific virus was used, which lacked the second mitochondrial promotor. Removing this second promotor should allow expression in the whole cell, and thus increase the probability for neurons to express the FRET sensor.

However, the results show the opposite (Fig. 3.9), after 4 weeks only a few cells were visible in the cortex and the hippocampus. After 5 weeks no increase in virus expressing cells was visible. The few positive cells were again all at big arterioles. In the SOC no cells were expressed at all. As consequence of these results, the focus was set on the mitochondrial AAVs for the first ATP measurements.

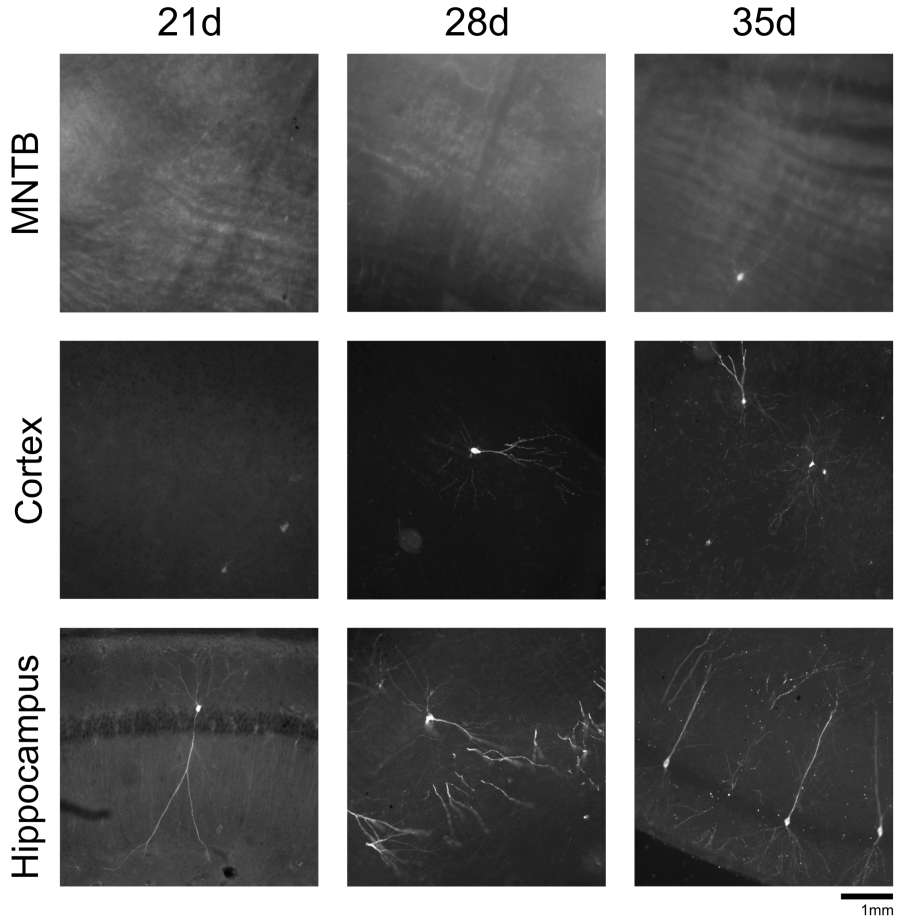

Figure 3.7: Expression of ATeam in mitochondria *3 different brain regions MNTB, cortex and hippocampus and 3, 4 and 5 weeks of transduction with mitochondrial AAVs. Brain slices are 60 (Cortex and Hippocampus) or 200µm (MNTB) thick.*

3.2.2 *Detection of ATeam1.03^{YEMK}*

Detecting fluorescence changes from cortical brain slices after simulation was possible. In both channels (CFP and mVenus) a signal was visible, which would accord with a transient increase in ATP concentration (Fig. 3.10A). However, a negative control with a wild-type animal exhibited the same fluorescence changes (Fig. 3.10B). Studying the fluorescence spectra (Fig. 1.3) suggests that it is likely that the visible signal occurs from NADH and FAD autofluorescence changes that would also be detected with the ATP filters.

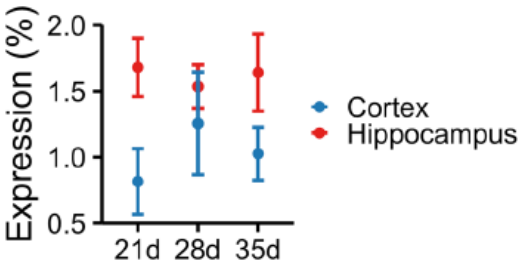

Figure 3.8: *Percentage of cells expressing ATeam1.03^{YEMK} in the mitochondria after different expression times. (Per area there were between 50 and 120 neuron and maximal 2 neurons expressed the sensor) Mean ± SEM; number of different areas n=10*

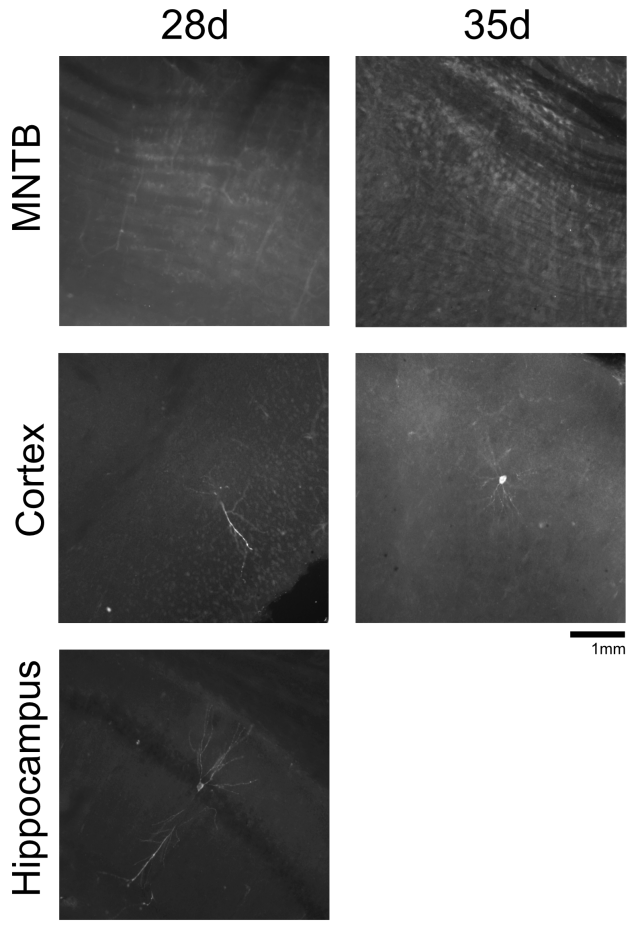

Figure 3.9: ***Expression of cytosolic AAV*** *Different brain regions (MNTB, cortex and hippocampus) after 4 and after 5 weeks of expression. Brain slices are 60 (MNTB 35d, cortex 28d, hippocampus) or 200µm (MNTB 28d, cortex 35d) thick.*

To test whether it is possible to detect ATP changes, the slices were superfused with 10µM of ATP while recording the fluorescence. The results

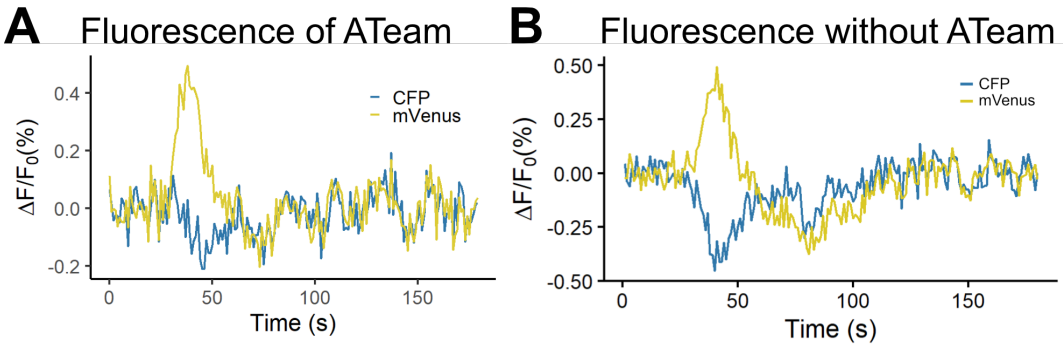

Figure 3.10: Fluorescence of CFP and mVenus channel after stimulation *(200Hz, 400 stimuli) (A) In the cortex after an expression time of 5 weeks. (B) Negative control: captured fluorescence in the cortex of a wild-type animal.*

show only in the CFP channel an increase in the fluorescence (Fig. 3.11A). The reason for such a response cannot be due to the FRET sensor since an increase in ATP concentration should decrease the CFP fluorescence. A control experiment with a wild-type animal revealed that this assumption holds true, since a similar result was found (Fig. 3.11B). The reason for the fluorescence change is due to autofluorescence changes instead of the FRET sensor.

The final conclusion of this project is that it is possible to express the ATP FRET sensor ATeam1.03^{YEMK} via systemically applied AAVs in the Mongolian gerbil. However, so far not enough cells are expressing the ATP FRET sensor after 5 weeks to measure ATP levels.

3.3 THE MODEL

3.3.1 *Dynamic Flux Balance Analysis*

As a first start, the model of DiNuzzo et al. (2017) was used with all reactions they implemented. This model contained a neuron and an astrocyte, both with two compartments (cytosol and mitochondria). Besides the important metabolic pathways for both cell types (glycolysis, TCA, OxPhos) this model contained the lactate shuttle, pyruvate recycling (malic enzyme (ME)), mitochondrial carriers and NADH shuttles, ammonia homeostasis,

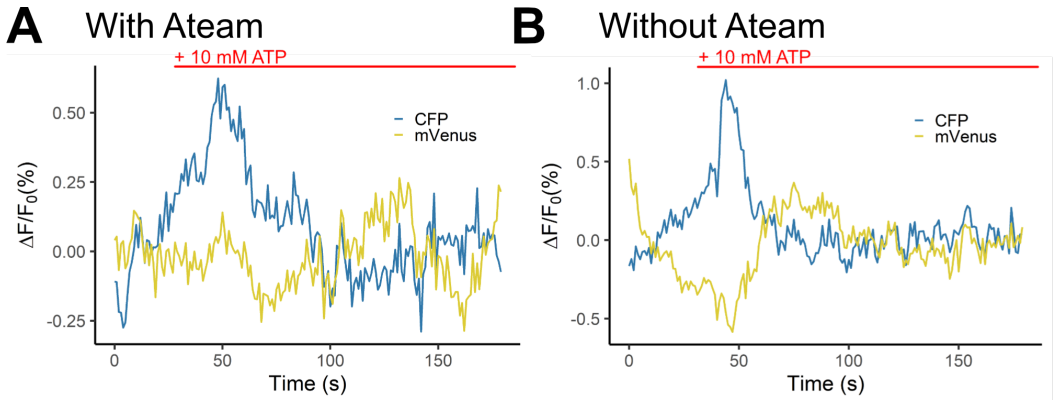

Figure 3.11: Fluorescence of CFP and mVenus channel after wash in of 10mM of ATP *(A) In the cortex after an expression time of 5 weeks. (B) Negative control: captured fluorescence in the cortex of a wild-type animal.*

antioxidant system, synaptic transmission (glutamate release and recycling, Na-K-pump). In total, this model has 122 reactions with 124 metabolites. The only difference to the published model was to include FAD and $FADH_2$ as metabolite and add it to some reactions instead of NAD/NADH (e.g. SDH produces $FADH_2$ instead of 2/3 NADH). With this slightly changed model and an objective function that minimises the neuronal uptake of O_2, glucose and lactate a first analysis with the MATLAB scripts of Dromms et al. (2020) was possible. The system was perturbed after 30s for 5s by increasing the lower bound of the neuronal transmission, this resulted in an increase of the OxPhos but not of the glycolysis. The problem with this quick analysis was that the model was not in a steady state before or after the stimulation. Big fluctuations in metabolite concentrations were visible. Since it was not possible to achieve a steady state with this combination of reactions and boundaries the model was implemented again with ODEs.

3.3.2 *The way to the final model*

Initially, also by implementing ODEs no steady state was achieved, for this reason I reduced the number of reactions in several steps. This reduced also the number of parameters drastically. The final model contains 30 reactions with 80 parameters and 33 metabolites (Fig. 2.4 or Appendix) and it was possible to achieve a steady state of the system with the given starting concentration. This is a crucial step to justify the model, since without a steady state it is not possible to trust any results.

3.3.3 *Sensitivity Analysis*

The following sensitivity analysis of the kinetic parameters revealed the following parameters as important for the system. The parameters were divided into those belonging to cytosolic reaction, mitochondrial reactions, and to transporters. A threshold of 0.06 was used and all parameters with a sensitivity above this threshold were classified as sensitive parameters, all below the threshold are not sensitive (Fig. 3.12). The analysis reveals that the transport reactions are sensitive, especially the O_2 diffusion, as well as the housekeeping mechanisms. For cytosolic reactions mainly the lactate dehydrogenase (LDH), pyruvate dehydrogenase (PDH) and the phosphofructokinase (PFK) are sensitive, while for mitochondrial reactions mainly the OxPhos and the α-ketogluterate dehydrogenase show high sensitivity.

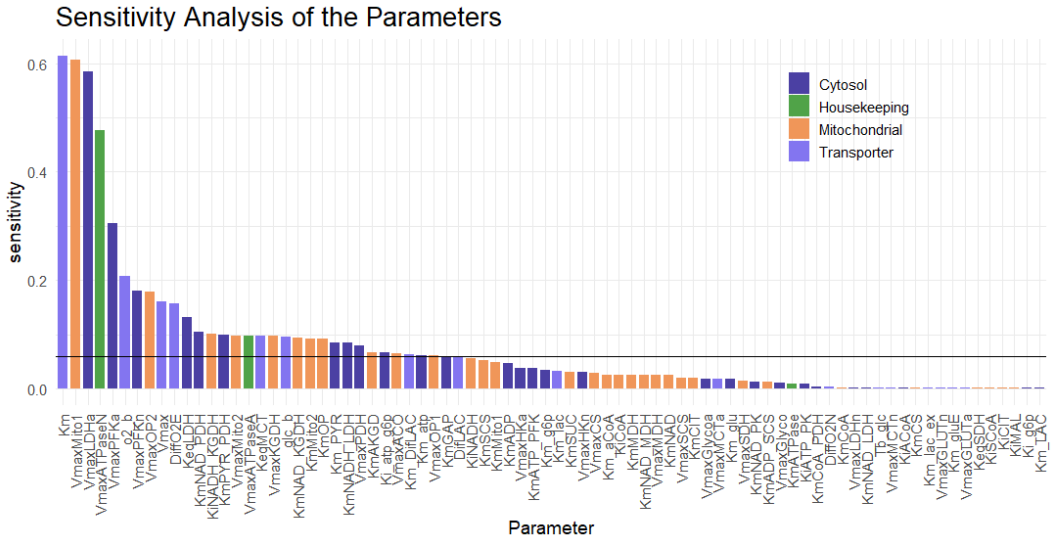

Figure 3.12: Sensitivity analysis *with a threshold at 0.06. The colour of the bars show if the parameter belong to a cytosolic, mitochondrial or a transport reaction or to a housekeeping process. To which reaction a parameter belongs can be checked in the Appendix*

3.3.4 *Functionality - proof of principle*

For the proof of principle, I pertubated the system with an ATP pulse after 15 sec, this resulted in an increase in FAD levels and a decrease in NADH and O_2 levels similar to the experimental results (Fig. 3.13). After

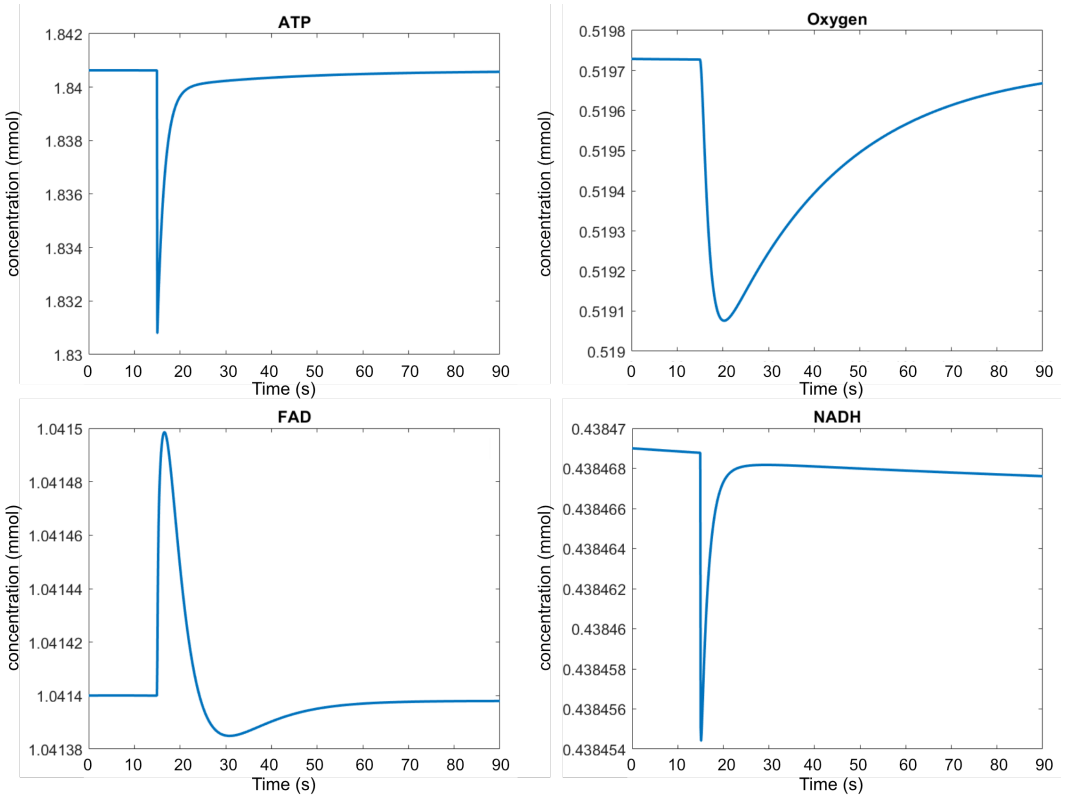

Figure 3.13: Model Simulation *with an ATP puls after 15 sec. O_2 and FAD curve is exactly as in experiments. NADH curve shows a oxidation of NADH to NAD^+ as in experiments.*

the perturbation the concentrations asymptotically return to the starting concentration. FAD and O_2 have a different time course, exactly as in the experiments. The NADH time course is not the same as in the experiments, but NADH is consumed as in the autofluorescence measurements. Even though this is not a final validation of the model, it shows that the model is on the right track. With a few changes of some parameters the NADH curve should become more similar to the experiments.

4

DISCUSSION

4.1 NADH AND FAD AUTOFLUORESCENCE MEASUREMENTS

NADH and FAD autofluorescence measurements have the advantage to be a non-invasive method to monitor relative changes in NADH and FAD levels with a temporal resolution in the range of seconds. However, it is just an indirect track of the ATP regeneration in brain slices, and the question arises, which metabolic processes are reflected by these changes? A widespread interpretation of the time course of NADH and FAD in neuronal tissue can be explained in two phases (Shuttleworth, 2010). The first phase starts with an increase of FAD and a decrease of NADH levels, which reflects the ATP regeneration mainly via OxPhos. In the second phase, NADH and $FADH_2$ levels need to be recovered which often leads to an overshoot (Fig. 2.1) (Shuttleworth, 2010, Brosel et al., 2018). According to literature, this second phase is caused by glycolysis, lactate shuttle or TCA cycle. Since NADH autofluorescence originates by 90% from mitochondria, and FAD is mainly found in mitochondrial processes (Shuttleworth, 2010), the TCA cycle is most likely the source for the recovery of NADH and $FADH_2$ detected by autofluorescence imaging.

4.1.1 *Astrocytic Contribution*

An astrocytic contribution to the autofluorescence levels can not be excluded but is unlikely. Autofluorescence of NADH produced during the glycolysis of astrocytes can be neglected since this takes place in the cytoplasm. The

same holds true for the oxidation of NADH by the LDH to produce lactate. The OxPhos of astrocytes does not increase their rates during the firing of neurons, therefore, detectable NADH and FAD autofluorescence levels stay unchanged (Rose et al., 2020).

4.1.2 *Parameters to analyse autofluorescence changes*

The most common parameters determined from autofluorescence curves are the peak amplitude and the overshoot of the time series. Also other parameters can be determined as shown in Fig. 2.1. In the following, I discuss the different parameters I extracted from the time series data:

- **Amplitude:** The difference between the baseline and the maximal oxidation level of the two dinucleotides. At this point the oxidation rate of NADH/$FADH_2$ (first phase) equals the reduction rate of NAD^+/FAD (second phase) for a short time. It is the standard readout for autofluorescence measurements (Shuttleworth, 2010).

- **Time to the peak:** Shows how long it takes until the peak is reached (oxidation and reduction rate become equal).

- **Integral:** Depends on all parameters and is an indicator of the overall consumption of ATP.

- **Overshoot:** Shows how much NADH/$FADH_2$ is overproduced by the second phase, before the levels return to a baseline. It has several interpretations by different groups, according to the fact that the main source of the fluorescence origins from the mitochondria it is most likely that the neuronal TCA cycle is the reason for the overshoot (Shuttleworth, 2010).

4.2 METABOLIC FREQUENCY DEPENDENCE

4.2.1 *Impact of OxPhos*

The consumption of O_2 helps to get a more detailed image of the OxPhos. The experiments demonstrated that the O_2 consumption stays constant for lower frequencies and decreases for higher frequencies (Fig. 3.2). This suggests a reducing contribution of the OxPhos for increasing frequencies. The question remains why the O_2 amplitudes stay constant for frequencies up to 100 Hz while the amplitudes of NADH and FAD curves are increasing. One possible explanation for this phenomenon is a faster second phase of the autofluorescence curves compared to the back-diffusion of O_2 through the slice to the active region. The integral of the autofluorescence changes as indicator of the total ATP consumption shows a similar image as the O_2 amplitudes. In this case, the changes of both metabolites favour the strong contribution of OxPhos for ATP production.

The inhibition of complex I, III and IV of the OxPhos shows its importance during firing. A strong reduction of the autofluorescence amplitude is observed, which recovers partially after the washout of the blockers (Fig. 3.3). This supports the importance of OxPhos for low frequencies. A more detailed conclusion from this data is not possible, because:

(1) The inhibition can lead to a reduction in firing frequency which can result in a false correlation. Even if the MNTB neurons themselves would be able to continue firing, the Calyx of Held is known to increase its failure rate while blocking of OxPhos (Lujan et al., 2021).

(2) The cell is forced to use different pathways to compensate for the missing ATP production from OxPhos.

4.2.2 *Firing pattern*

Three different firing patterns were used to stimulate the MNTB neurons: 5s stimulation, 400 stimuli and burst stimulation. With these it was possible to compare the metabolic need of different firing patterns.

5s stimulation

A fixed stimulation period leads to an increasing signal of NADH and FAD time series. This suggests an increasing demand for ATP due to the rising number of APs up to 200Hz. This observation fits to the findings of Brosel et al. (2018) in the LSO. Two possible reasons can explain why the amplitude does not rise further after 200 Hz:

(1) The number of triggered APs does not rise further due to spike failures (Kopp-Scheinpflug et al., 2003) and, thus, the ATP consumption does not increase further.

(2) The OxPhos is not as important for higher frequencies as for lower frequencies, other pathways become more important.

400 stimuli

The second firing pattern tries to test these potential explanations. With a fixed number of 400 stimuli, the ATP demand of the neurons for APs should stay constant, if the firing frequency is not relevant. The results show that for lower frequencies the amplitudes increase similar to the 5s stimulation. While for higher frequencies > 200 Hz the amplitude decreases with increasing frequency. This decrease suggests that the ATP-generating pathway changes from OxPhos to a different one, for example, glycolysis.

Burst stimulation

The computational study of Yi and Grill (2019) showed that the firing pattern of thalamo-cortical relay neurons does affect their metabolic needs. To test this in MNTB neurons the cells were stimulated with bursts in different frequencies. Experiments with the described burst mode showed no significant difference in autofluorescence amplitude. In contrast to the integral that was significantly larger for half of the frequencies (NADH: 200 Hz, 800 Hz, 1000 Hz; FAD: 200 Hz, 400 Hz, 1000 Hz). This observation indicates a higher ATP consumption for these frequencies, which could be explained by decreased failure rate due to the breaks between two bursts. Still, since the tendency stays the same, the integral decreases with increasing frequency. This supports the idea of a decreasing contribution of the OxPhos for higher frequencies.

4.2.3 *Context*

To bring the results into a bigger context I try to describe which steps are happening in the MNTB. When an AP arrives at the Calyx of Held vesicles with glutamate are released to the synaptic cleft to transmit the signal to the MNTB neurons. The astrocytes close to the synaptic cleft take up some glutamate and the glycolysis is increased (Castro et al., 2009). This results in an overproduction of lactate that is released into the extracellular space where neurons do take up the lactate, and transform it into pyruvate that fuels the TCA cycle. This way the glycolysis and the TCA cycle become uncoupled and an optimal energy supply for different circumstances becomes possible, also the astrocytes can help to optimal control the NAD^+/NADH-ratio (Rabinowitz and Enerbäck, 2020). With this help from the astrocytes the mitochondria can sufficiently supply the neuron at lower frequencies with ATP. For higher frequencies, a faster energy supply becomes more relevant and the neurons switch their metabolism more towards glycolysis for a quick energy supply. Without the astrocytes and their lactate shuttle, the glycolysis of neurons would be increased a lot to produce the necessary pyruvate by itself.

4.3 GLUCOSE AVAILABILITY

For most experiments shown here the ACSF solution contained 2mM of glucose (Brosel et al., 2018), which is a physiological concentration in vascularised brain tissue. Most experiments in literature use a higher glucose concentration (often around 10mM). By providing a high glucose concentration they aim for a good nutrient supply of the cells, despite the slow diffusion of the nutrients through the tissue. However, non-physiological glucose concentrations can shift the relevance of the different pathways. An increased glucose availability can lead to mechanisms like the Crabtree effect (Barros et al., 2021) and the flux of glycolysis increases despite a sufficient O_2 supply. Even though some systems apparently have a higher need for glucose (Hollnagel et al., 2020), in the MNTB a reliable firing rate of 300Hz could be shown with a glucose concentration of 1mM (Lujan et al., 2021).

The data suggest that the increased glucose concentration leads to a reduced NADH overshoot and FAD amplitude. A possible reason for the difference in the overshoot could be an increased baseline. However, without further experiments this possibility can not be fully excluded. Another interpretation is that at 10mM glucose concentrations, the neurons increase the flux of glycolysis and reduce the use of the TCA cycle. This increased production of pyruvate might also increase lactate generation, which would consume NADH. Both can explain a reduced overshoot. The latter can also explain the reduced FAD amplitude. Surprisingly, the NADH amplitude does not decrease significantly, this could be explained by a high pyruvate availability that leads to an increased NADH oxidation by the LDH. This might have a small impact on the NADH autofluorescence. Overall, an increase in glycolysis and LDH activity and a reduction in mitochondrial processes can explain the observed effects.

4.4 ESTABLISHMENT OF AN ATP SENSOR

NADH and FAD levels are only an indirect measurement of the energy consumption. Other additional experimental readouts would be helpful for a better understanding and to improve and evaluate the model. An interesting approach would be to measure the ATP levels directly, which can be achieved with an ATP FRET sensor (Imamura et al., 2009).

Imamura et al. (2009) developed a FRET sensor for real-time tracking of ATP in living cells called ATeam1.03^{YEMK}. Lerchundi et al. (2019) showed that this biosensor is able to track ATP in neurons and astrocytes. They recorded from organotypic brain slice culture and Gerkau et al. (2019) also from acute brain slices of the hippocampus. With sodium imaging and the detection of ATP changes, Gerkau et al. (2019) studied the relation between activity induced Na^+ influx and ATP. They observed an ATP consumption, by the NKA to recover from global Na^+ influx, that exceeds ATP production. When the Na^+ was only local and the ATP production was fast enough, no drop of ATP could be observed (Gerkau et al., 2019).

4.4.1 *New systematical application in Mongolian gerbils*

So far, ATeam1.03^{YEMK} was only expressed in different mouse and rat lines or cell cultures. In Chapter 3 it is shown that a systemic application through the V. femoralis in the Mongolian gerbil is possible, even though some aspects still need improvement. The first step was done to establish a FRET sensor in Mongolian gerbils. Most AAVs barely cross the BBB and a stereotactical injection is necessary, the used capsid AAV-PHP.eB has the ability to cross the BBB in some mouse lines (e.g. C57BL/6J), while in others this is not possible (e.g. BALB/cJ) (Chan et al., 2017, Hordeaux et al., 2019). The results in Chapter 3 show that AAV-PHP.eB crosses the BBB in Mongolian gerbils and a systemic application is possible. In mice a systemical application is achieved via the tail vein, this is not possible for Mongolian gerbils because their tail is hirsute and the tail vein is barely visible. For this reason, the systemic application was achieved via the V. femoralis. The systemical application reduces the suffering of the animals compared to a stereotactical application. Additionally, it has the advantage that ATeam1.03^{YEMK} should be expressed in all brain areas and different regions can be researched. Even though the systemic application in the Mongolian gerbil is possible, not enough cells expressed the sensor to measure changes in ATP levels. The few virus-positive cells showed an all-or-nothing expression, this rises the assumption that only a few neurons were transduced but these got a high dose of AAVs.

4.5 THE MODEL

The final model is a rather simple description of our system. Although, the DFBA was not able to find a biologically relevant solution, the ODE model with drastically reduced reactions and parameters was able to find a steady state. A sensitivity analysis showed that the model parameters of the OxPhos, transport and housekeeping reactions as well as the PFK, LDH, PDH and AKGDH showed a high sensitivity. The sensitivity of these reactions is in accordance with their importance for this system, which shows that the model seems to be realistic. The PFK is a rate-limiting enzyme in glycolysis (Boscá and Corredor, 1984, Mergenthaler et al., 2013). The AKGDH is thought to be a rate-limiting enzyme in the TCA cycle and its decrease is associated with neurodegenerative diseases (Gibson et al.,

2003). The transport reactions are necessary to fuel the reactions and the OxPhos.

First trials to perturbate the model with ATP pulses (to mimic APs) showed changes in FAD, O_2 and NADH levels that are very similar to experimental measurements. Even though such a stimulation is no validation of the model, it shows that the model is on the right track and is able to come back to a steady state after perturbation.

4.5.1 *Similarities and differences to other models*

A similar but much more detailed model was developed by Berndt et al. (2015). They simulated the tissue of a brain slice to be as close as possible to the *in-vitro* situation. This is an important aspect that is especially necessary when the model helps in the interpretation of data. In the model presented here this aspect was kept, by modelling a diffusion of oxygen and glucose.

Most models in literature do not distinguish between NADH and $FADH_2$. Since FAD is one of the few readouts of the described experiments it is crucial to include both dinucleotides in the model.

4.6 POSSIBLE EXPERIMENTAL IMPROVEMENTS

Our experimental design has some drawbacks that can be resolved for future experiments. Other limitations cannot be improved by better experimental design, but the model should solve these problems.

4.6.1 *Gender differences*

In my study I used both females and males for the experiments, which might increase the variance of the data points. Since there are differences in male and female energy metabolism, it is possible that the analysis would be a little different if one distinguishes between males and females. With some more experiments, one could reanalyse the data to search for gender differences.

4.6.2 *Influence of temperature*

When researching biochemical systems, temperature is an important aspect. The speed of reactions is changing and neurons fire less reliably at non-physiological temperature (Grande and Wang, 2011). Ibrahim et al. (2017) showed the effect of temperature (in the range between 13 and 37°C) on autofluorescence curves of NADH and FAD. They observe a less pronounced second phase the lower the temperature is while the peak amplitude is even more pronounced. For the interpretation of the autofluorescence data, this needs to be kept in mind. While the body temperature of amphibians depends on their surrounding temperature, the Mongolian gerbil has a stable body temperature between 36°C and 39°C. In future experiments, it could be interesting to change the model organism and compare the impact of temperature in amphibians. For further experiments in Mongolian gerbils or mice the temperature for the experiments should be increased to 36°C. However, this comes with the disadvantage that cells in acute brain slices die much faster at higher temperatures. For long experimental paradigms, like in the study presented here with 8 different frequencies and 5 min breaks between stimulations for recovery, this can lead to problems. A reduction in autofluorescence amplitude could occur for later stimulations due to a reduced number of responding neurons.

4.6.3 *Oxygen availability in experiments*

Oxygen availability in brain slices is also an issue that should be improved for further experiments. In acute brain slices, blood vessels are no longer capable of supplying the cells with oxygen and other essential nutrients. Diffusion from the ACSF through several cell layers takes much more time, which is a problem for neurons that need a fast oxygen supply. Experiments that change the ambient oxygen concentration reveal the impact on oxygen availability. A reduced oxygen supply increases the NADH autofluorescence baseline, while the integral decreased significantly and the overshoot of the NADH signal increased (Galeffi et al., 2011). Ivanov and Zilberter (2011) have demonstrated the importance of a sufficient oxygen availability and how a reduced oxygen supply changes the autofluorescence signals as well as the firing behaviour of the cells. According to their results, a perfusion rate of 15 ml/min is necessary for an appropriate oxygenation of a brain slice, otherwise, the NADH autofluorescence amplitude decreases as well

as the O_2 amplitude and the amount of available O_2. The perfusion rate in our setup was slower (0.45 ml/min). However, since there is still O_2 in the slices after stimulation it can be assumed that the O_2 supply is not limiting the OxPhos. Still, the O_2 supply can be improved for deeper cell layers, for example with thicker tubes or by increasing the speed of the pump. Moreover, the big round perfusion chamber is suboptimal for an optimised oxygen supply. In a chamber with a large surface, O_2 leaves more easily into the air. Ivanov and Zilberter (2011) designed a perfusion chamber that minimises oxygen escape, this chamber has a volume < 1 ml and a dual laminar flow. This chamber increases oxygen availability significantly, especially for deeper cell layers. Designing such a chamber for our setup might improve oxygen supply.

Another possible solution was shown by Özugur et al. (2021). They were able to increase O_2 concentration in brain and rescue neuronal activity in a hypoxic environment, by injecting microalgae into the heart of *Xenupus laevis* tadpoles (details on the experimental protocol are found in Özugur et al. (2022)). After vascular distribution of the microorganism, illumination lead to photosynthesis by the algae and increased the oxygen concentration. This seems to be the first step to improve the oxygen supply in acute brain slices and solves the problem of slow diffusion from ACSF solution into deeper tissue layers. Further development will be necessary to find a suitable solution for mice tissue. Such a development could solve problems with oxygen availability in brain slices. A disadvantage of such an approach is that a combination with autofluorescence imaging will be difficult to achieve, since it is crucial for autofluorescence imaging to avoid any light pollution and to reduce photobleaching of the slices.

4.6.4 *Actual firing rate*

Even though the cells were stimulated with frequencies up to 1000Hz, the stimulation rate is likely not the actual firing rate. Since no recording of the APs of the MNTB cells was performed, published literature is necessary to estimate the actual firing rate of the neurons for higher frequencies in the presented experiments. As mentioned in the Introduction, MNTB principal cells are able to have firing rates up to 1000Hz (Kopp-Scheinpflug et al., 2003), but such high firing frequencies are achieved only under special conditions at physiological temperature. Up to 300 Hz, MNTB

principal neurons are reliably firing at the same frequency as the stimulation (Taschenberger and Von Gersdorff, 2000, Kopp-Scheinpflug et al., 2003). For these frequencies (10 Hz - 200 Hz), experiments with fixed stimulation duration and those with a fixed number of stimuli show similar results of increasing amplitudes for increasing frequency. This supports the suggestion that increasing frequencies elevates the flux of OxPhos.

For frequencies above 200 Hz, it needs to be considered that a mismatch between the stimulation rate and the actual firing rate can occur. The autofluorescence amplitudes decrease under stimulation with 400 impulses. This decrease could be explained either by a metabolic switch or by an increasing failure rate of the neurons. As the MNTB is electrophysiologically well-studied (Taschenberger and Von Gersdorff, 2000, von Gersdorff and Borst, 2002, Kopp-Scheinpflug et al., 2003, Grande and Wang, 2011, Borst and Soria Van Hoeve, 2012) the failure rate can be estimated. Since the autofluorescence experiments are non-invasive it is necessary to estimate the failure rate according to measurements that do not change the intracellular composition (e.g. cell-attached or in-vivo recordings). A rather simple estimation was done in Fig. 3.5. The estimation of the amplitude per AP revealed two different images for the experiments with 5s stimulation and 400 stimuli. For increasing frequency, the amplitude per AP increases with the 400 stimuli protocol, while it decreases for the 5s stimulation. The similarity between the two estimations is that more APs lead to a decreased amplitude per AP. This observation can have two possible explanations:

(1) The ATP consumption increases per single AP the fewer APs in total are triggered

(2) The neurons switch from glycolysis to OxPhos the fewer APs in total are triggered and with it the amplitude per AP gets bigger

4.6.5 *Improving expression of ATeam1.03^{YEMK}*

A first step to establish an ATP FRET-sensor in the Mongolian gerbil was done. Still, there are problems to solve in order to obtain a working system for measuring ATP levels in the neurons and especially in the auditory brainstem. First of all, the virus needs to be expressed in the whole tissue not only close to big arterioles. To address this issue it could help to do

an infusion instead of an injection. With an infusion, the same amount of AAVs will be introduced to the system in a longer time period, this should lead to a better distribution in the whole brain. Hence, it might have the advantage of a more efficient viral expression in the brainstem since the distribution of blood vessels is different in different brain regions. Another possibility is to change the capsid, a new capsid AAV PHP.N is now available which is neuron-specific (Kumar et al., 2020). With this capsid, a ubiquitous promotor (e.g. CAG) could be used that shows a better expression for neurons in the SOC. Hordeaux et al. (2019) showed that the virus expression is dependent on the mouse strain. Therefore, to be sure that it is not a gerbil-specific problem it would be helpful to inject the virus via the V. femoralis to a mouse line that is known to have no problems in expressing AAV-PHP.eB, for example, C5BL/6J. The presented results show an all-or-nothing expression, this tells that maybe not the expression time was the problem and with an improved virus or virus application, it would be possible to reduce the expression time.

4.7 CONCLUSION

In conclusion, NADH and FAD autofluorescence imaging were used, as well as O_2 measurements, to explore the frequency dependence of metabolic processes in MNTB neurons. Indeed, a metabolic adaptation to the broad firing frequency of these neurons was found. Also, the amount of available glucose has an impact on the used metabolic pathways but not the stimulation pattern. The MNTB neurons are switching the contribution of glycolysis and OxPhos depending on the stimulation frequency. These findings are also relevant for other neurons capable of high firing frequencies (Wang et al., 2016, Ritzau-Jost et al., 2014). For a more detailed analysis of the pathways with direct insights into ATP consumption and production, an ATP FRET sensor could be established. For ATP measurements further improvements need to be done, but a systemic application in Mongolian gerbils is possible. Finally, I developed a model that can be utilised after validation for the interpretation of experimental data, providing insights into the metabolic adaptations that occur in response to neuronal activity. First tests show that the model is in a steady state that is reached again after perturbation with an ATP pulse. The concentrations of NADH but especially FAD and O_2 show very similar behaviour as measured in the

experiments after electrical stimulation. The study of metabolic adaptions to neuronal activity will help to improve the interpretation of functional neuroimaging data by knowing the individual metabolic adaptations of different neuron types. Understanding the relationship between metabolism and electrical activity of various neuron types might help to use NADH/-FAD autofluorescence lifetime imaging microscopy (FLIM) in the future as a new diagnostic tool for neurodegenerative diseases (Chakraborty et al., 2016, Shi et al., 2017).

4.8 FUTURE WORK

There are many directions in which one can continue the work. Since I started some projects that I could not finish, these are good starting points for future projects. There are two parts for the following work: the experimental and the theoretical work. Both are worthy and interesting to investigate further. In the experimental part the FRET-sensor can give new insights into the metabolism of MNTB neurons and the data that can be fed to the model. The downside of FRET sensors in general are a high sensitivity to temperature and pH value as well as different bleaching of the two fluorophores. Because of these problems, one has to be careful with interpretations of measured data with ATeam1.03^{YEMK}. Before continuing this project it is recommendable to wait for improved forms of an ATP biosensor.

On the other hand, the modelling part can be continued. A validation of the model with experiments would be the next step. If the model is indeed valid it is possible to perturb the system in the same way as the brain slices were stimulated. This will help for further interpretation. It might also be possible to return to the FBA, but more information is necessary to justify an objective function. The mathematical model will help to find better boundaries for the fluxes of the FBA and with that the possible solution space becomes smaller. The model will help to determine interesting pathways and with it the next direction for experiments.

BIBLIOGRAPHY

A. Aubert and R. Costalat. Interaction between astrocytes and neurons studied using a mathematical model of compartmentalized energy metabolism. *Journal of Cerebral Blood Flow and Metabolism*, 25(11):1476–1490, 2005. doi: 10.1038/sj.jcbfm.9600144. URL https://doi.org/10.1038/sj.jcbfm.9600144. PMID: 15931164.

F. Baeza-Lehnert, A. S. Saab, R. Gutiérrez, V. Larenas, E. Díaz, M. Horn, M. Vargas, L. Hösli, J. Stobart, J. Hirrlinger, B. Weber, and L. F. Barros. Non-canonical control of neuronal energy status by the na + pump. *Cell Metabolism*, 29:668–680.e4, 3 2019. ISSN 19327420. doi: 10.1016/j.cmet.2018.11.005.

L. K. Bak, A. B. Walls, A. Schousboe, A. Ring, U. Sonnewald, and H. S. Waagepetersen. Neuronal glucose but not lactate utilization is positively correlated with nmda-induced neurotransmission and fluctuations in cytosolic ca^{2+} levels. *Journal of Neurochemistry*, 109:87–93, 5 2009. ISSN 00223042. doi: 10.1111/j.1471-4159.2009.05943.x.

M. Balestrino, M. Lensman, M. Parodi, L. Perasso, R. Rebaudo, R. Melani, S. Polenov, and A. Cupello. Role of creatine and phosphocreatine in neuronal protection from anoxic and ischemic damage. *Amino Acids*, 23 (1-3):221–229, sep 2002. ISSN 0939-4451. doi: 10.1007/s00726-001-0133-3. URL http://link.springer.com/10.1007/s00726-001-0133-3.

L. F. Barros, I. Ruminot, A. San Martín, R. Lerchundi, I. Fernández-Moncada, and F. Baeza-Lehnert. Aerobic Glycolysis in the Brain: Warburg and Crabtree Contra Pasteur. *Neurochemical Research*, 46(1):15–22, jan 2021. ISSN 0364-3190. doi: 10.1007/s11064-020-02964-w. URL http://link.springer.com/10.1007/s11064-020-02964-w.

M. Bélanger, I. Allaman, and P. J. Magistretti. Brain Energy Metabolism: Focus on Astrocyte-Neuron Metabolic Cooperation. *Cell Metabolism*, 14(6):

724–738, dec 2011. ISSN 15504131. doi: 10.1016/j.cmet.2011.08.016. URL https://linkinghub.elsevier.com/retrieve/pii/S1550413111004207.

J. M. Berg, J. L. Tymoczko, G. J. Gatto, and L. Stryer. *Stryer Biochemie*. Springer Berlin Heidelberg, 2018. ISBN 978-3-662-54619-2. doi: 10.1007/978-3-662-54620-8. URL http://link.springer.com/10.1007/978-3-662-54620-8.

N. Berndt. *Theoretische Untersuchungen zur Kopplung von neuronaler Erregung und neuronalem Energiestoffwechsel*. Dissertation, 2012. pages 62-96.

N. Berndt, O. Kann, and H.-G. Holzhütter. Physiology-Based Kinetic Modeling of Neuronal Energy Metabolism Unravels the Molecular Basis of NAD(P)H Fluorescence Transients. *Journal of Cerebral Blood Flow Metabolism*, 35(9):1494–1506, sep 2015. ISSN 0271-678X. doi: 10.1038/jcbfm.2015.70. URL http://journals.sagepub.com/doi/10.1038/jcbfm.2015.70.

J. G. G. Borst and J. Soria Van Hoeve. The calyx of held synapse: From model synapse to auditory relay. *Annual Review of Physiology*, 74:199–224, 2012. ISSN 00664278. doi: 10.1146/annurev-physiol-020911-153236.

L. Boscá and C. Corredor. Is phosphofructokinase the rate-limiting step of glycolysis? *Trends in Biochemical Sciences*, 9:372–373, 9 1984. ISSN 09680004. doi: 10.1016/0968-0004(84)90214-7. URL https://linkinghub.elsevier.com/retrieve/pii/0968000484902147.

S. Brosel, B. Grothe, and L. Kunz. An auditory brainstem nucleus as a model system for neuronal metabolic demands. *European Journal of Neuroscience*, 47(3):222–235, feb 2018. ISSN 0953816X. doi: 10.1111/ejn.13789. URL https://onlinelibrary.wiley.com/doi/10.1111/ejn.13789.

S. Camandola and M. P. Mattson. Brain metabolism in health, aging, and neurodegeneration. *The EMBO Journal*, 36(11):1474–1492, 2017. doi: https://doi.org/10.15252/embj.201695810. URL https://www.embopress.org/doi/abs/10.15252/embj.201695810.

M. A. Castro, F. A. Beltrán, S. Brauchi, and I. I. Concha. A metabolic switch in brain: glucose and lactate metabolism modulation by ascorbic acid. *Journal of Neurochemistry*, 110(2):423–440, jul 2009. ISSN 00223042. doi: 10.1111/j.1471-4159.2009.06151.x. URL http://doi.wiley.com/10.1111/j.1471-4159.2009.06151.x.

S. Cerdán, T. B. Rodrigues, A. Sierra, M. Benito, L. L. Fonseca, C. P. Fonseca, and M. L. García-Martín. The redox switch/redox coupling hypothesis. *Neurochemistry International*, 48(6):523–530, 2006. ISSN 0197-0186. doi: https://doi.org/10.1016/j.neuint.2005.12.036. URL https://www.sciencedirect.com/science/article/pii/S0197018606000477. Glutamate in CNS Metabolism and Neurotransmission: Interactions at the Inter and Intracellular Level.

S. Chakraborty, F.-S. Nian, J.-W. Tsai, A. Karmenyan, and A. Chiou. Quantification of the metabolic state in cell-model of parkinson's disease by fluorescence lifetime imaging microscopy. *Scientific Reports*, 6:19145, 2016. ISSN 2045-2322. doi: 10.1038/srep19145. URL https://doi.org/10.1038/srep19145.

K. Y. Chan, M. J. Jang, B. B. Yoo, A. Greenbaum, N. Ravi, W.-L. Wu, L. Sánchez-Guardado, C. Lois, S. K. Mazmanian, B. E. Deverman, and V. Gradinaru. Engineered aavs for efficient noninvasive gene delivery to the central and peripheral nervous systems. *Nature Neuroscience*, 20: 1172–1179, 8 2017. ISSN 1097-6256. doi: 10.1038/nn.4593.

B. Chance and H. Baltscheffsky. Respiratory enzymes in oxidative phosphorylation. vii. binding of intramitochondrial reduced pyridine nucleotide. *The Journal of biological chemistry*, 233:736–9, 9 1958. ISSN 0021-9258. URL http://www.ncbi.nlm.nih.gov/pubmed/13575447.

Y.-T. Chen, Y.-C. Lee, Y.-H. Lai, J.-C. Lim, N.-T. Huang, C.-T. Lin, and J.-J. Huang. Review of integrated optical biosensors for point-of-care applications. *Biosensors*, 10(12), 2020. ISSN 2079-6374. doi: 10.3390/bios10120209. URL https://www.mdpi.com/2079-6374/10/12/209.

S. Cheng, Y. Fu, Y. Zhang, W. Xian, H. Wang, B. Grothe, X. Liu, X. Xu, A. Klug, and E. A. McCullagh. Enhancement of de novo sequencing, assembly and annotation of the mongolian gerbil genome with transcrip-

tome sequencing and assembly from several different tissues. *BMC Genomics*, 20:903, 12 2019. ISSN 1471-2164. doi: 10.1186/s12864-019-6276-y. URL https://bmcgenomics.biomedcentral.com/articles/10.1186/s12864-019-6276-y.

N. Choudhury, D. Linley, A. Richardson, M. Anderson, S. W. Robinson, V. Marra, V. Ciampani, S. M. Walter, C. Kopp-Scheinpflug, J. R. Steinert, and I. D. Forsythe. Kv3.1 and kv3.3 subunits differentially contribute to kv3 channels and action potential repolarization in principal neurons of the auditory brainstem. *The Journal of Physiology*, 598(11):2199–2222, 2020. doi: https://doi.org/10.1113/JP279668. URL https://physoc.onlinelibrary.wiley.com/doi/abs/10.1113/JP279668.

L. C. Clark and C. Lyons. Electrode systems for continuous monitoring in cardiovascular surgery. *Annals of the New York Academy of Sciences*, 102: 29–45, 12 1962. ISSN 00778923. doi: 10.1111/j.1749-6632.1962.tb13623.x. URL https://onlinelibrary.wiley.com/doi/10.1111/j.1749-6632.1962.tb13623.x.

R. D. Dayton, M. S. Grames, and R. L. Klein. More expansive gene transfer to the rat CNS: AAV PHP.EB vector dose–response and comparison to AAV PHP.B. *Gene Therapy*, 25(5):392–400, 2018. ISSN 14765462. doi: 10.1038/s41434-018-0028-5. URL http://dx.doi.org/10.1038/s41434-018-0028-5.

G. Descalzi, V. Gao, M. Q. Steinman, A. Suzuki, and C. M. Alberini. Lactate from astrocytes fuels learning-induced mrna translation in excitatory and inhibitory neurons. *Communications Biology*, 2:247, 7 2019. ISSN 2399-3642. doi: 10.1038/s42003-019-0495-2.

C. M. Díaz-García, D. J. Meyer, N. Nathwani, M. Rahman, J. R. Martínez-François, and G. Yellen. The distinct roles of calcium in rapid control of neuronal glycolysis and the tricarboxylic acid cycle. *eLife*, 10:1–30, feb 2021. ISSN 2050084X. doi: 10.7554/eLife.64821. URL https://elifesciences.org/articles/64821.

G. A. Dienel. Brain glucose metabolism: Integration of energetics with function. *Physiological Reviews*, 99(1):949–1045, 2019. doi: 10.1152/

physrev.00062.2017. URL https://doi.org/10.1152/physrev.00062.2017. PMID: 30565508.

M. DiNuzzo, F. Giove, B. Maraviglia, and S. Mangia. Computational Flux Balance Analysis Predicts that Stimulation of Energy Metabolism in Astrocytes and their Metabolic Interactions with Neurons Depend on Uptake of K+ Rather than Glutamate. *Neurochemical Research*, 42(1): 202–216, 2017. ISSN 15736903. doi: 10.1007/s11064-016-2048-0. URL http://dx.doi.org/10.1007/s11064-016-2048-0.

S. Direnberger, R. Banchi, S. Brosel, C. Seebacher, S. Laimgruber, R. Uhl, F. Felmy, H. Straka, and L. Kunz. Analysis of signal processing in vestibular circuits with a novel light-emitting diodes-based fluorescence microscope. *European Journal of Neuroscience*, 41(10):1332–1344, 5 2015. ISSN 0953816X. doi: 10.1111/ejn.12907. URL http://doi.wiley.com/10.1111/ejn.12907.

T. M. Donnelly and F. W. Quimby. Biology and Diseases of Other Rodents, 2002. URL https://linkinghub.elsevier.com/retrieve/pii/B9780122639517500107.

R. A. Dromms, J. Y. Lee, and M. P. Styczynski. LK-DFBA: a linear programming-based modeling strategy for capturing dynamics and metabolite-dependent regulation in metabolism. *BMC Bioinformatics*, 21 (1):93, dec 2020. ISSN 1471-2105. doi: 10.1186/s12859-020-3422-0. URL https://bmcbioinformatics.biomedcentral.com/articles/10.1186/s12859-020-3422-0.

M. R. Duchen. Ca2+-dependent changes in the mitochondrial energetics in single dissociated mouse sensory neurons. *Biochemical Journal*, 283(1):41–50, apr 1992. ISSN 0264-6021. doi: 10.1042/bj2830041. URL https://portlandpress.com/biochemj/article/283/1/41/27085/Ca2-dependent-changes-in-the-mitochondrial.

C. Fang, Y. Huang, and Y. Zhao. Review of fret biosensing and its application in biomolecular detection. *American journal of translational research*, 15:694–709, 2023. ISSN 1943-8141. URL http://www.ncbi.nlm.nih.gov/pubmed/36915763http://www.pubmedcentral.nih.gov/articlerender.fcgi?artid=PMC10006758.

I. Fernández-Moncada, I. Ruminot, D. Robles-Maldonado, K. Alegría, J. W. Deitmer, and L. F. Barros. Neuronal control of astrocytic respiration through a variant of the crabtree effect. *Proceedings of the National Academy of Sciences*, 115:1623–1628, 2 2018. ISSN 0027-8424. doi: 10.1073/pnas.1716469115.

M. C. Ford, O. Alexandrova, L. Cossell, A. Stange-Marten, J. Sinclair, C. Kopp-Scheinpflug, M. Pecka, D. Attwell, and B. Grothe. Tuning of Ranvier node and internode properties in myelinated axons to adjust action potential timing. *Nature Communications*, 6(1):8073, aug 2015. ISSN 2041-1723. doi: 10.1038/ncomms9073. URL https://www.nature.com/articles/ncomms9073.

A. G. Forderhase, H. C. Styers, C. A. Lee, and L. A. Sombers. Simultaneous voltammetric detection of glucose and lactate fluctuations in rat striatum evoked by electrical stimulation of the midbrain. *Analytical and Bioanalytical Chemistry*, 412(24):6611–6624, sep 2020. ISSN 16182650. doi: 10.1007/s00216-020-02797-0. URL https://link.springer.com/10.1007/s00216-020-02797-0.

F. Galeffi, G. G. Somjen, K. A. Foster, and D. A. Turner. Simultaneous Monitoring of Tissue Po 2 and NADH Fluorescence During Synaptic Stimulation and Spreading Depression Reveals a Transient Dissociation between Oxygen Utilization and Mitochondrial Redox State in Rat Hippocampal Slices. *Journal of Cerebral Blood Flow & Metabolism*, 31(2): 626–639, feb 2011. ISSN 0271-678X. doi: 10.1038/jcbfm.2010.136. URL http://journals.sagepub.com/doi/10.1038/jcbfm.2010.136.

M. I. Gaviria-Arroyave, J. B. Cano, and G. A. Peñuela. Nanomaterial-based fluorescent biosensors for monitoring environmental pollutants: A critical review. *Talanta Open*, 2:100006, 12 2020. ISSN 26668319. doi: 10.1016/j.talo.2020.100006.

S. Genc, I. A. Kurnaz, and M. Ozilgen. Astrocyte - neuron lactate shuttle may boost more ATP supply to the neuron under hypoxic conditions - in silico study supported by in vitro expression data. *BMC Systems Biology*, 5(1):162, 2011. ISSN 1752-0509. doi: 10.1186/1752-0509-5-162. URL http://bmcsystbiol.biomedcentral.com/articles/10.1186/1752-0509-5-162.

N. J. Gerkau, R. Lerchundi, J. S. E. Nelson, M. Lantermann, J. Meyer, J. Hirrlinger, and C. R. Rose. Relation between activity-induced intracellular sodium transients and atp dynamics in mouse hippocampal neurons. *The Journal of Physiology*, 597:5687–5705, 12 2019. ISSN 0022-3751. doi: 10.1113/JP278658. URL https://onlinelibrary.wiley.com/doi/10.1113/JP278658.

G. Gibson, A. Kingsbury, H. Xu, J. Lindsay, S. Daniel, O. Foster, A. Lees, and J. Blass. Deficits in a tricarboxylic acid cycle enzyme in brains from patients with parkinson's disease. *Neurochemistry International*, 43:129–135, 7 2003. ISSN 01970186. doi: 10.1016/S0197-0186(02)00225-5. URL https://linkinghub.elsevier.com/retrieve/pii/S0197018602002255.

G. Grande and L. Y. Wang. Morphological and functional continuum underlying heterogeneity in the spiking fidelity at the calyx of held synapse in vitro. *Journal of Neuroscience*, 2011. ISSN 02706474. doi: 10.1523/JNEUROSCI.0400-11.2011.

B. Grothe, M. Pecka, and D. McAlpine. Mechanisms of sound localization in mammals. *Physiological Reviews*, 90(3):983–1012, 2010. ISSN 00319333. doi: 10.1152/physrev.00026.2009.

Y. Hayakawa, T. Nemoto, M. Iino, and H. Kasai. Rapid ca2+-dependent increase in oxygen consumption by mitochondria in single mammalian central neurons. *Cell Calcium*, 37:359–370, 4 2005. ISSN 01434160. doi: 10.1016/j.ceca.2004.11.005.

H. Hirase, X. Leinekugel, A. Czurkó, J. Csicsvari, and G. Buzsáki. Firing rates of hippocampal neurons are preserved during subsequent sleep episodes and modified by novel awake experience. *Proceedings of the National Academy of Sciences*, 98:9386–9390, 7 2001. ISSN 0027-8424. doi: 10.1073/pnas.161274398. URL https://pnas.org/doi/full/10.1073/pnas.161274398.

B. K. Hoffpauir, D. R. Kolson, P. H. Mathers, and G. A. Spirou. Maturation of synaptic partners: functional phenotype and synaptic organization tuned in synchrony. *The Journal of Physiology*, 588:4365–4385, 11 2010. ISSN 00223751. doi: 10.1113/jphysiol.2010.198564. URL http://doi.wiley.com/10.1113/jphysiol.2010.198564.

J.-O. Hollnagel, T. Cesetti, J. Schneider, A. Vazetdinova, F. Valiullina-Rakhmatullina, A. Lewen, A. Rozov, and O. Kann. Lactate attenuates synaptic transmission and affects brain rhythms featuring high energy expenditure. *iScience*, 23:101316, 7 2020. ISSN 25890042. doi: 10.1016/j.isci.2020.101316. URL https://linkinghub.elsevier.com/retrieve/pii/S2589004220305034.

J. Hordeaux, Y. Yuan, P. M. Clark, Q. Wang, R. A. Martino, J. J. Sims, P. Bell, A. Raymond, W. L. Stanford, and J. M. Wilson. The gpi-linked protein ly6a drives aav-php.b transport across the blood-brain barrier. *Molecular Therapy*, 27(5):912–921, 2019. ISSN 1525-0016. doi: https://doi.org/10.1016/j.ymthe.2019.02.013. URL https://www.sciencedirect.com/science/article/pii/S1525001619300541.

C. Howarth, P. Gleeson, and D. Attwell. Updated energy budgets for neural computation in the neocortex and cerebellum. *Journal of Cerebral Blood Flow & Metabolism*, 32(7):1222–1232, 2012. doi: 10.1038/jcbfm.2012.35. URL https://doi.org/10.1038/jcbfm.2012.35. PMID: 22434069.

S. Hoyer. Abnormalities of glucose metabolism in Alzheimer's disease. In *Annals of the New York Academy of Sciences*, 1991. doi: 10.1111/j.1749-6632.1991.tb00190.x.

C. Huchzermeyer, K. Albus, H.-J. Gabriel, J. Otáhal, N. Taubenberger, U. Heinemann, R. Kovács, and O. Kann. Gamma oscillations and spontaneous network activity in the hippocampus are highly sensitive to decreases in po2 and concomitant changes in mitochondrial redox state. *Journal of Neuroscience*, 28(5):1153–1162, 2008. ISSN 0270-6474. doi: 10.1523/JNEUROSCI.4105-07.2008. URL https://www.jneurosci.org/content/28/5/1153.

C. Huchzermeyer, N. Berndt, H.-G. Holzhütter, and O. Kann. Oxygen consumption rates during three different neuronal activity states in the hippocampal ca3 network. *Journal of Cerebral Blood Flow & Metabolism*, 33 (2):263–271, 2013. doi: 10.1038/jcbfm.2012.165. URL https://doi.org/10.1038/jcbfm.2012.165. PMID: 23168532.

B. A. Ibrahim, H. Wang, A. M. Lesicko, B. Bucci, K. Paul, and D. A. Llano. Effect of temperature on FAD and NADH-derived signals and neu-

rometabolic coupling in the mouse auditory and motor cortex. *Pflugers Archiv European Journal of Physiology*, 469(12):1631–1649, 2017. ISSN 14322013. doi: 10.1007/s00424-017-2037-4.

H. Imamura, K. P. Huynh Nhat, H. Togawa, K. Saito, R. Iino, Y. Kato-Yamada, T. Nagai, and H. Noji. Visualization of atp levels inside single living cells with fluorescence resonance energy transfer-based genetically encoded indicators. *Proceedings of the National Academy of Sciences*, 106(37):15651–15656, 2009. ISSN 0027-8424. doi: 10.1073/pnas.0904764106. URL https://www.pnas.org/content/106/37/15651.

T. M. Inc. Matlab version: 9.11.0 (r2021b), 2021. URL https://www.mathworks.com.

A. Ivanov and Y. Zilberter. Critical state of energy metabolism in brain slices: The principal role of oxygen delivery and energy substrates in shaping neuronal activity. *Frontiers in Neuroenergetics*, 2011. ISSN 16626427. doi: 10.3389/fnene.2011.00009.

M. K. Jha and B. M. Morrison. Glia-neuron energy metabolism in health and diseases: New insights into the role of nervous system metabolic transporters. *Experimental Neurology*, 309:23–31, nov 2018. ISSN 00144886. doi: 10.1016/j.expneurol.2018.07.009. URL https://linkinghub.elsevier.com/retrieve/pii/S0014488618302504.

M. K. Jha and B. M. Morrison. Lactate transporters mediate glia-neuron metabolic crosstalk in homeostasis and disease. *Frontiers in Cellular Neuroscience*, 14, 2020. ISSN 1662-5102. doi: 10.3389/fncel.2020.589582. URL https://www.frontiersin.org/article/10.3389/fncel.2020.589582.

C. Kopp-Scheinpflug, W. R. Lippe, G. J. Dörrscheidt, and R. Rübsamen. The medial nucleus of the trapezoid body in the gerbil is more than a relay: Comparison of pre- and postsynaptic activity. *JARO - Journal of the Association for Research in Otolaryngology*, 2003. ISSN 15253961. doi: 10.1007/s10162-002-2010-5.

C. Kopp-Scheinpflug, J. R. Steinert, and I. D. Forsythe. Modulation and control of synaptic transmission across the mntb. *Hearing Research*, 279 (1):22–31, 2011. ISSN 0378-5955. doi: https://doi.org/10.1016/j.heares.

2011.02.007. URL https://www.sciencedirect.com/science/article/pii/S0378595511000438. Synaptic Plasticity.

D. E. Kuhl, E. J. Metter, and W. H. Riege. Patterns of local cerebral glucose utilization determined in Parkinson's disease by the [18F]fluorodeoxyglucose method. *Annals of Neurology*, pages 419–424, 1984. ISSN 15318249. doi: 10.1002/ana.410150504.

S. R. Kumar, T. F. Miles, X. Chen, D. Brown, T. Dobreva, Q. Huang, X. Ding, Y. Luo, P. H. Einarsson, A. Greenbaum, M. J. Jang, B. E. Deverman, and V. Gradinaru. Multiplexed cre-dependent selection yields systemic aavs for targeting distinct brain cell types. *Nature Methods*, 17: 541–550, 5 2020. ISSN 1548-7091. doi: 10.1038/s41592-020-0799-7.

R. Lerchundi, K. W. Kafitz, U. Winkler, M. Färfers, J. Hirrlinger, and C. R. Rose. Fret-based imaging of intracellular atp in organotypic brain slices. *Journal of Neuroscience Research*, 97:933–945, 8 2019. ISSN 0360-4012. doi: 10.1002/jnr.24361. URL https://onlinelibrary.wiley.com/doi/10.1002/jnr.24361.

R. Lerchundi, N. Huang, and C. R. Rose. Quantitative Imaging of Changes in Astrocytic and Neuronal Adenosine Triphosphate Using Two Different Variants of ATeam. *Frontiers in Cellular Neuroscience*, 14(April):1–13, apr 2020. ISSN 1662-5102. doi: 10.3389/fncel.2020.00080. URL https://www.frontiersin.org/article/10.3389/fncel.2020.00080/full.

S. Li and Z. H. Sheng. Energy matters: presynaptic metabolism and the maintenance of synaptic transmission. *Nature Reviews Neuroscience*, 23(1): 4–22, 2022. ISSN 14710048. doi: 10.1038/s41583-021-00535-8.

S. J. Lucas, C. B. Michel, V. Marra, J. L. Smalley, M. H. Hennig, B. P. Graham, and I. D. Forsythe. Glucose and lactate as metabolic constraints on presynaptic transmission at an excitatory synapse. *The Journal of Physiology*, 596(9):1699–1721, may 2018. ISSN 0022-3751. doi: 10.1113/JP275107. URL https://onlinelibrary.wiley.com/doi/10.1113/JP275107https://physoc.onlinelibrary.wiley.com/doi/10.1113/JP275107.

B. Lujan, C. Kushmerick, T. D. Banerjee, R. K. Dagda, and R. Renden. Glycolysis selectively shapes the presynaptic action potential waveform. *Jour-*

nal of neurophysiology, 116(6):2523–2540, dec 2016. ISSN 1522-1598. doi: 10.1152/jn.00629.2016. URL https://www.physiology.org/doi/10.1152/jn.00629.2016http://www.ncbi.nlm.nih.gov/pubmed/27605535http://www.pubmedcentral.nih.gov/articlerender.fcgi?artid=PMC5133309.

B. J. Lujan, M. Singh, A. Singh, and R. B. Renden. Developmental shift to mitochondrial respiration for energetic support of sustained transmission during maturation at the calyx of Held. *Journal of Neurophysiology*, (8):976–996, 2021. ISSN 0022-3077. doi: 10.1152/jn.00333.2021.

P. J. Magistretti and I. Allaman. A cellular perspective on brain energy metabolism and functional imaging. *Neuron*, 86(4):883–901, may 2015. ISSN 1097-4199. doi: 10.1016/j.neuron.2015.03.035. URL http://www.ncbi.nlm.nih.gov/pubmed/25996133.

R. Mahadevan, J. S. Edwards, and F. J. Doyle. Dynamic flux balance analysis of diauxic growth in escherichia coli. *Biophysical Journal*, 83:1331–1340, 9 2002. ISSN 00063495. doi: 10.1016/S0006-3495(02)73903-9. URL https://linkinghub.elsevier.com/retrieve/pii/S0006349502739039.

G. Mayorga-Weber, F. J. Rivera, and M. A. Castro. Neuron-glia (mis)interactions in brain energy metabolism during aging. *Journal of Neuroscience Research*, 100:835–854, 3 2022. ISSN 0360-4012. doi: 10.1002/jnr.25015. URL https://onlinelibrary.wiley.com/doi/10.1002/jnr.25015.

P. Mergenthaler, U. Lindauer, G. A. Dienel, and A. Meisel. Sugar for the brain: the role of glucose in physiological and pathological brain function. *Trends in Neurosciences*, 36:587–597, 10 2013. ISSN 01662236. doi: 10.1016/j.tins.2013.07.001. URL https://linkinghub.elsevier.com/retrieve/pii/S0166223613001306.

D. J. Meyer, C. M. Díaz-García, N. Nathwani, M. Rahman, and G. Yellen. The na^+/k^+ pump dominates control of glycolysis in hippocampal dentate granule cells. *eLife*, 11:e81645, oct 2022. ISSN 2050-084X. doi: 10.7554/eLife.81645. URL https://doi.org/10.7554/eLife.81645.

P. Mächler, M. Wyss, M. Elsayed, J. Stobart, R. Gutierrez, A. von Faber Castell, V. Kaelin, M. Zuend, A. San Martín, I. Romero-Gómez, F. Baeza-

Lehnert, S. Lengacher, B. Schneider, P. Aebischer, P. Magistretti, L. Barros, and B. Weber. In vivo evidence for a lactate gradient from astrocytes to neurons. *Cell Metabolism*, 23:94–102, 1 2016. ISSN 15504131. doi: 10.1016/j.cmet.2015.10.010. URL https://linkinghub.elsevier.com/retrieve/pii/S1550413115005264.

J. D. Orth, I. Thiele, and B. Ø. Palsson. What is flux balance analysis? *Nature Biotechnology*, 28(3):245–248, mar 2010. ISSN 1087-0156. doi: 10.1038/nbt.1614. URL http://www.nature.com/articles/nbt.1614.

S. Özugur, M. N. Chávez, R. Sanchez-Gonzalez, L. Kunz, J. Nickelsen, and H. Straka. Green oxygen power plants in the brain rescue neuronal activity. *iScience*, 24:103158, 10 2021. ISSN 25890042. doi: 10.1016/j.isci.2021.103158. URL https://linkinghub.elsevier.com/retrieve/pii/S2589004221011263.

S. Özugur, M. N. Chávez, R. Sanchez-Gonzalez, L. Kunz, J. Nickelsen, and H. Straka. Transcardial injection and vascular distribution of microalgae in xenopus laevis as means to supply the brain with photosynthetic oxygen. *STAR Protocols*, 3:101250, 6 2022. ISSN 26661667. doi: 10.1016/j.xpro.2022.101250. URL https://linkinghub.elsevier.com/retrieve/pii/S2666166722001307.

N. Palandt, C. Resch, P. Unterlechner, L. Voshagen, V. Winhart, and L. Kunz. Metabolic adaptation of auditory neurons to their broad range of action potential frequencies. 2023. Manuscript under revision.

Y.-Z. Pan, T. P. Sutula, and P. A. Rutecki. 2-deoxy-d-glucose reduces epileptiform activity by presynaptic mechanisms. *Journal of Neurophysiology*, 121(4):1092–1101, 2019. doi: 10.1152/jn.00723.2018. URL https://doi.org/10.1152/jn.00723.2018. PMID: 30673364.

L. Pellerin and P. J. Magistretti. Glutamate uptake into astrocytes stimulates aerobic glycolysis: a mechanism coupling neuronal activity to glucose utilization. *Proceedings of the National Academy of Sciences*, 91(22):10625–10629, 1994. doi: 10.1073/pnas.91.22.10625. URL https://www.pnas.org/doi/abs/10.1073/pnas.91.22.10625.

C. C. Pérez-Garcõ, M. Peña-Penabad, M. J. Cano-Rábano, M. B. Garcõ, D. Gallego-Morales, M. A. Rios-Granja, and I. Diez-Prieto. A simple procedure to perform intravenous injections in the mongolian gerbil (meriones unguiculatus), 2003.

R Core Team. *R: A Language and Environment for Statistical Computing*. R Foundation for Statistical Computing, Vienna, Austria, 2022. URL https://www.R-project.org/.

J. D. Rabinowitz and S. Enerbäck. Lactate: the ugly duckling of energy metabolism. *Nature metabolism*, 2(7):566–571, jul 2020. ISSN 2522-5812. doi: 10.1038/s42255-020-0243-4. URL http://dx.doi.org/10.1038/s42255-020-0243-4https://www.nature.com/articles/s42255-020-0243-4http://www.ncbi.nlm.nih.gov/pubmed/32694798http://www.pubmedcentral.nih.gov/articlerender.fcgi?artid=PMC7983055.

V. Rackayova, C. Cudalbu, P. J. Pouwels, and O. Braissant. Creatine in the central nervous system: From magnetic resonance spectroscopy to creatine deficiencies. *Analytical Biochemistry*, 529:144–157, jul 2017. ISSN 00032697. doi: 10.1016/j.ab.2016.11.007. URL https://linkinghub.elsevier.com/retrieve/pii/S000326971630389X.

A. Ritzau-Jost, I. Delvendahl, A. Rings, N. Byczkowicz, H. Harada, R. Shigemoto, J. Hirrlinger, J. Eilers, and S. Hallermann. Ultrafast action potentials mediate kilohertz signaling at a central synapse. *Neuron*, 84(1):152–163, 2014. ISSN 0896-6273. doi: https://doi.org/10.1016/j.neuron.2014.08.036. URL https://www.sciencedirect.com/science/article/pii/S0896627314007375.

J. Rose, C. Brian, A. Pappa, M. I. Panayiotidis, and R. Franco. Mitochondrial metabolism in astrocytes regulates brain bioenergetics, neurotransmission and redox balance. *Frontiers in Neuroscience*, 14, 2020. ISSN 1662-453X. doi: 10.3389/fnins.2020.536682. URL https://www.frontiersin.org/articles/10.3389/fnins.2020.536682.

A. Ryan. Hearing sensitivity of the mongolian gerbil, Meriones unguiculatis. *Journal of the Acoustical Society of America*, 59(5):1222–1226, 1976.

ISSN NA. doi: 10.1121/1.380961. URL http://scitation.aip.org/content/asa/journal/jasa/59/5/10.1121/1.380961.

P. M. Schaefer, S. Kalinina, A. Rueck, C. A. von Arnim, and B. von Einem. NADH Autofluorescence-A Marker on its Way to Boost Bioenergetic Research. *Cytometry Part A*, 95(1):34–46, jan 2019. ISSN 15524922. doi: 10.1002/cyto.a.23597. URL https://onlinelibrary.wiley.com/doi/10.1002/cyto.a.23597.

R. Scholz, R. G. Thurman, J. R. Williamson, B. Chance, and T. Bücher. Flavin and pyridine nucleotide oxidation-reduction changes in perfused rat liver. i. anoxia and subcellular localization of fluorescent flavoproteins. *The Journal of biological chemistry*, 244:2317–24, 5 1969. ISSN 0021-9258.

F. Scott, P. Wilson, R. Conejeros, and V. S. Vassiliadis. Simulation and optimization of dynamic flux balance analysis models using an interior point method reformulation. *Computers and Chemical Engineering*, 119:152–170, 11 2018. ISSN 00981354. doi: 10.1016/j.compchemeng.2018.08.041. URL https://linkinghub.elsevier.com/retrieve/pii/S0098135418309190.

L. Shi, L. Lu, G. Harvey, T. Harvey, A. Rodríguez-Contreras, and R. R. Alfano. Label-free fluorescence spectroscopy for detecting key biomolecules in brain tissue from a mouse model of alzheimer's disease. *Scientific Reports*, 7:2599, 2017. ISSN 2045-2322. doi: 10.1038/s41598-017-02673-5. URL https://doi.org/10.1038/s41598-017-02673-5.

C. W. Shuttleworth. Use of NAD(P)H and flavoprotein autofluorescence transients to probe neuron and astrocyte responses to synaptic activation. *Neurochemistry International*, 56(3):379–386, 2 2010. ISSN 01970186. doi: 10.1016/j.neuint.2009.12.015. URL https://linkinghub.elsevier.com/retrieve/pii/S0197018609003398.

L. Sokoloff. Localization of functional activity in the central nervous system by measurement of glucose utilization with radioactive deoxyglucose. *Journal of Cerebral Blood Flow and Metabolism*, 1:7–36, 3 1981. ISSN 0271678X. doi: 10.1038/jcbfm.1981.4. URL http://journals.sagepub.com/doi/10.1038/jcbfm.1981.4. PMID: 7035471.

E. Somersalo, Y. Cheng, and D. Calvetti. The metabolism of neurons and astrocytes through mathematical models. *Annals of Biomedical Engineering*, 40:2328–2344, 11 2012. ISSN 00906964. doi: 10.1007/s10439-012-0643-z.

H. Taschenberger and H. Von Gersdorff. Fine-tuning an auditory synapse for speed and fidelity: Developmental changes in presynaptic waveform, EPSC kinetics, and synaptic plasticity. *Journal of Neuroscience*, 2000. ISSN 02706474. doi: 10.1523/jneurosci.20-24-09162.2000.

B. Trattner, C. M. Gravot, B. Grothe, and L. Kunz. Metabolic Maturation of Auditory Neurones in the Superior Olivary Complex. *PLoS ONE*, 8(6): e67351, 6 2013. ISSN 1932-6203. doi: 10.1371/journal.pone.0067351. URL https://dx.plos.org/10.1371/journal.pone.0067351.

S. Vijayan, G. J. Hale, C. I. Moore, E. N. Brown, and M. Wilson. Activity in the barrel cortex during active behavior and sleep. *Journal of Neurophysiology*, 103(4):2074–2084, 2010. doi: 10.1152/jn.00474.2009. URL https://doi.org/10.1152/jn.00474.2009. PMID: 20164403.

E. P. Vining. Clinical efficacy of the ketogenic diet. *Epilepsy Research*, 37(3):181–190, 1999. ISSN 0920-1211. URL https://www.sciencedirect.com/science/article/pii/S0920121199000704. DOI: https://doi.org/10.1016/S0920-1211(99)00070-4.

H. von Gersdorff and J. G. G. Borst. Short-term plasticity at the calyx of held. *Nature Reviews Neuroscience*, 3(1):53–64, 2002. ISSN 14710048. doi: 10.1038/nrn705.

G. A. Wagnieres, W. M. Star, and B. C. Wilson. In vivo fluorescence spectroscopy and imaging for oncological applications. *Photochemistry and Photobiology*, 68(5):603–632, 1998. doi: https://doi.org/10.1111/j.1751-1097.1998.tb02521.x. URL https://onlinelibrary.wiley.com/doi/abs/10.1111/j.1751-1097.1998.tb02521.x.

B. Wang, W. Ke, J. Guang, G. Chen, L. Yin, S. Deng, Q. He, Y. Liu, T. He, R. Zheng, Y. Jiang, X. Zhang, T. Li, G. Luan, H. D. Lu, M. Zhang, X. Zhang, and Y. Shu. Firing frequency maxima of fast-spiking neurons in human, monkey, and mouse neocortex. *Frontiers in Cellular Neuroscience*, 10(OCT2016), oct 2016. ISSN 16625102. doi:

10.3389/fncel.2016.00239. URL http://journal.frontiersin.org/article/10.3389/fncel.2016.00239/full.

L.-Y. Wang, L. Gan, I. D. Forsythe, and L. K. Kaczmarek. Contribution of the kv3.1 potassium channel to high-frequency firing in mouse auditory neurones. *The Journal of Physiology*, 509(1):183–194, 1998. doi: https://doi.org/10.1111/j.1469-7793.1998.183bo.x. URL https://physoc.onlinelibrary.wiley.com/doi/abs/10.1111/j.1469-7793.1998.183bo.x.

G. Yellen. Fueling thought: Management of glycolysis and oxidative phosphorylation in neuronal metabolism. *Journal of Cell Biology*, 217(7):2235–2246, jul 2018. ISSN 0021-9525. doi: 10.1083/jcb.201803152. URL https://rupress.org/jcb/article/217/7/2235/39109/Fueling-thought-Management-of-glycolysis-and.

G. Yi and W. M. Grill. Average firing rate rather than temporal pattern determines metabolic cost of activity in thalamocortical relay neurons. *Scientific Reports*, 9(1):6940, dec 2019. ISSN 2045-2322. doi: 10.1038/s41598-019-43460-8. URL http://www.nature.com/articles/s41598-019-43460-8.

M. Zuend, A. S. Saab, M. T. Wyss, K. D. Ferrari, L. Hösli, Z. J. Looser, J. L. Stobart, J. Duran, J. J. Guinovart, L. F. Barros, and B. Weber. Arousal-induced cortical activity triggers lactate release from astrocytes. *Nature Metabolism*, 2:179–191, 2020. ISSN 25225812. doi: 10.1038/s42255-020-0170-4. URL http://dx.doi.org/10.1038/s42255-020-0170-4.

APPENDIX

1 BLEED-THROUGH CORRECTION

To simultaneously measure NADH and FAD in the same experiment, a multiband filter set was used. This led to the excitation of FAD at 360nm and resulted in the issue of FAD autofluorescence bleeding through into the NADH fluorescence channel. NADH images were rectified for the impact of FAD autofluorescence with the following method. it was possible to calculate the FAD contribution for excitation at 365nm (FAD365) from the pure FAD image obtained with excitation at 470nm (FAD470), by utilizing the LED spectra (d), the peak intensities of the LEDs (LED365, LED470), FAD absorption spectrum (f), and transmission spectrum of the excitation filter (e).

$$\begin{aligned} FAD_{365} &= \frac{LED_{365} * \int_{365}^{417} d * e * f d\lambda}{LED_{470} * \int_{365}^{417} d * e * f d\lambda} * FAD_{470} \\ &= 0.796 * FAD_{470} \end{aligned}$$

Afterwards, the autofluorescence image from NADH alone ($NADH_{real}$)was obtained by subtracting the FAD365 contribution from the measured NADH autofluorescence image.

$$NADH_{real} = NADH_{365} - FAD_{365} = NADH_{365} - 0.796 * FAD_{470}$$

A validation of the bleed-through correction method was performed by measuring the autofluorescence of three solutions containing 150µM of

NADH with varying concentrations of FAD (0 μM, 20 μM, and 40 μM). After applying the bleed-through correction, NADH autofluorescence values were obtained that were consistent with the expectations from the same NADH concentration in all three solutions. The measured autofluorescence values exhibit significant differences compared to the values obtained without FAD, highlighting the importance of applying a correction method.

FAD concentration	measured NADH autofluorescence	corrected NADH autofluorescence
0 μM	241	241
20 μM	381	213
40 μM	479	186

2 KINETICS

The used kinetics for the computational model with Km as Michaelis-Menten constant and V_{max} as maximal rate of a reaction. All metabolites (and reactions) are marked in which compartment they are with the following abbreviations:

$$\begin{aligned} n &- \text{Neuron} \\ nc &- \text{Cytosol of Neuron} \\ nm &- \text{Mitochondria of Neuron} \\ a &- \text{Astrocyte} \\ e &- \text{extracellular} \end{aligned}$$

=> O_2^e: OxygenDif

$$vf = DiffO_2^e \times \left(O_2^b - O_2^e\right)$$

$$\begin{aligned} DiffO_2^e &= 0.04 \\ O_2^b &= 1 \end{aligned}$$

=> glu_n : GLUTn

$$vf = V_{max}^{GLUTn} \times \frac{glu_e - glu_n}{1 + \frac{glu_e}{Km_{gluE}} + \frac{glu_n}{Km_{gluE}}}$$

$$\begin{aligned} V_{max}^{GLUTn} &= 0.72 \\ Km_{gluE} &= 2.87 \\ glu_e &= 2 \end{aligned}$$

=> glu_a : GLUTa

$$vf = V_{max}^{GLUTa} \times \frac{glu_e}{1 + \frac{glu_e}{Km_{gluE}} + \frac{glu_a}{Km_{gluE}}}$$

$$V_{max}^{GLUTa} = 0.72$$
$$Km_{gluE} = 2.87$$
$$glu_e = 2$$

O_2^e => O_2^n : OxgenDifN (Oxygen Diffusion Neuron)

$$vf = DiffO_2^N \times (O_2^e - O_2^n)$$

$$DiffO_2^N = 0.5$$

atp_n+glu_n => adp_n+$g6p_n$: HKn

$$vf = V_{max}^{HKn} \times \frac{glu_n}{glu_n + Km_{glu}} \times \frac{atp_n}{atp_n + Km_{atp}\left(1 + \frac{g6p_n}{Ki_{atp}^{g6p}}\right)}$$

$$V_{max}^{HKn} = 9.36$$
$$Km_{glu} = 0.043$$
$$Km_{atp} = 0.37$$
$$Ki_{atp}^{g6p} = 7.4e-05$$

atp_n+$g6p_n$ => 2 gap_n+adp_n : PFKn

$$vf = V_{max}^{PFKn} \times \frac{g6p_n}{Km_{g6p} + g6p_n} \times \frac{atp_n}{atp_n + KmATP_{PFK}}$$

$$V_{max}^{PFKn} = 0.0026$$
$$Km_{g6p} = 0.027$$
$$KmATP_{PFK} = 0.055$$

gap_n+nad_{nc}+2 adp_n => $nadh_{nc}$+pyr_n+ 2 atp_n : Glyco2n

$$vf = V_{max}^{Glycon} \frac{gap_n}{gap_n + Km_{GAP}} \frac{nad_{nc}}{nad_{nc} + Km_{NAD}^{PK}} \frac{adp_n}{adp_n + Km_{ADP}\left(1 + \frac{atp_n}{Ki_{ATP}^{PK}}\right)}$$

$$V_{max}^{Glycon} = 23.76$$
$$Km_{GAP} = 0.074$$
$$Km_{NAD}^{PK} = 0.01$$
$$Km_{ADP} = 0.42$$
$$Ki_{ATP}^{PK} = 4.4$$

atp_a+glu_a => adp_a+$g6p_a$: HKa

$$vf = V_{max}^{HKa} \times \frac{glu_a}{glu_a + Km_{glu}} \times \frac{atp_a}{atp_a + Km_{atp}\left(1 + \frac{g6p_a}{Ki_{atp}^{g6p}}\right)}$$

$$V_{max}^{HKa} = 9.36$$
$$Km_{glu} = 0.043$$
$$Km_{atp} = 0.37$$
$$Ki_{atp}^{g6p} = 7.4e-05$$

atp_a+$g6p_a$ => adp_a+2*gap_a : PFKa

$$vf = V_{max}^{PFKa} \times \frac{g6p_a}{Km_{g6p} + g6p_a} \times \frac{atp_a}{atp_a + KmATP_{PFK}}$$

$$V_{max}^{PFKa} = 0.0026$$
$$Km_{g6p} = 0.027$$
$$KmATP_{PFK} = 0.055$$

2 adp_a+gap_a+nad_{ac} => 2 atp_a+$nadh_a$+pyr_a : Glyco2a

$$vf = V_{max}^{GlycoA} \frac{gap_a}{gap_a + Km_{GAPa}} \frac{nad_{ac}}{nad_{ac} + Km_{NAD}^{PKa}} \frac{adp_a}{adp_a + Km_{ADP}\left(1 + \frac{atp_a}{Ki_{ATP}^{PK}}\right)}$$

$$V_{max}^{GlycoA} = 23.76$$
$$Km_{GAP} = 0.074$$
$$Km_{NAD}^{PK} = 0.01$$
$$Km_{ADP} = 0.42$$
$$Ki_{ATP}^{PK} = 4.4$$

pyr_n+$nadh_{nc}$ <=> nad_{nc}+lac_n : LDHn

$$vf = \frac{V_{max}^{LDHn} \times pyr_n \times nadh_{nc}}{\left(1 + \frac{pyr_n}{Km_{PYR}}\right) \times \left(1 + \frac{nadh_{nc}}{KmNADH_{LDH}}\right) + \left(1 + \frac{lac_n}{Km_{LAC}}\right) \times \left(1 + \frac{nad_{nc}}{KmNAD_{LDH}}\right) - 1}$$

$$vr = \frac{V_{max}^{LDHn} \times lac_n \times \frac{nad_{nc}}{KeqLDH}}{\left(1 + \frac{pyr_n}{Km_{PYR}}\right) \times \left(1 + \frac{nadh_{nc}}{KmNADH_{LDH}}\right) + \left(1 + \frac{lac_n}{Km_{LAC}}\right) \times \left(1 + \frac{nad_{nc}}{KmNAD_{LDH}}\right) - 1}$$

$$V_{max}^{LDHn} = 100000$$
$$KeqLDH = 8400$$
$$Km_{PYR} = 0.36$$
$$Km_{LAC} = 4.2$$
$$KmNADH_{LDH} = 0.043$$
$$KmNAD_{LDH} = 0.088$$

lac_n <=> lac_e : MCTn

$$vf = V_{max}^{MCTn} \times \frac{lac_n}{\left(1 + \frac{lac_n}{Km_{lac}}\right) + \left(1 + \frac{lac_e}{Km_{lac_{ex}}}\right) - 1}$$

$$vr = V_{max}^{MCTn} \times \frac{\frac{lac_e}{K_{eq}^{MCT}}}{\left(1 + \frac{lac_n}{Km_{lac}}\right) + \left(1 + \frac{lac_e}{Km_{lac_{ex}}}\right) - 1}$$

$$V_{max}^{MCTn} = 5$$
$$Km_{lac} = 1.1$$
$$Km_{lac_{ex}} = 1.1$$
$$K_{eq}^{MCT} = 1.737$$

lac_a => lac_e : MCTa

$$vf = V_{max}^{MCTa} \times \frac{lac_a}{lac_a + Km_{lac}}$$

$$V_{max}^{MCTa} = 5$$
$$Km_{lac} = 1.1$$

$nadh_a$+pyr_a => lac_a+nad_ac : LDHa

$$vf = V_{max}^{LDHa} \times \frac{pyr_a}{Km_{PYR} + pyr_a} \times \frac{nadh_a}{Km_{NADH}^{LDH} + nadh_a}$$

$$V_{max}^{LDHa} = 100000$$
$$Km_{PYR} = 0.36$$
$$Km_{NADH}^{LDH} = 0.043$$

nad_nm+pyr_n+coA_n => $nadh_{nm}$+$aCoA_n$: PDHn

$$vf = V_{max}^{PDH} \times \frac{pyr_n}{pyr_n + Km_{PYR}^{PDH}} \times \frac{nad_{nm}}{nad_{nm} + Km_{NAD}^{PDH}} \times \frac{coA_n}{coA_n + Km_{CoA}^{PDH}\left(1 + \frac{aCoA_n}{Ki_{ACoA}}\right)}$$

$$V_{max}^{PDH} = 13.1$$
$$Km_{PYR}^{PDH} = 0.068$$
$$Km_{NAD}^{PDH} = 0.041$$
$$Km_{CoA}^{PDH} = 0.0047$$
$$Ki_{ACoA} = 0.0004$$

oaa_n+$aCoA_n$ => cit_n+coA_n : CSn

$$vf = V_{max}^{CS} \times \frac{oaa_n}{oaa_n + Km_{CS}\left(1 + \frac{cit_n}{Ki_{CIT}}\right)} \times \frac{aCoA_n}{aCoA_n + Km_{aCoA}\left(1 + \frac{coA_n}{Ki_{CoA}}\right)}$$

$$V_{max}^{CS} = 1280$$
$$Km_{CS} = 0.0045$$
$$Ki_{CIT} = 3.7$$
$$Km_{aCoA} = 0.005$$
$$Ki_{CoA} = 0.025$$

cit_n+nad_{nm} => akg_n+$nadh_{nm}$: ACOn

$$vf = V_{max}^{ACO} \times \frac{cit_n}{cit_n + Km_{CIT}} \times \frac{nad_{nm}}{nad_{nm} + Km_{NAD}\left(1 + \frac{nadh_{nm}}{Ki_{NADH}}\right)}$$

$$V_{max}^{ACO} = 64$$
$$Km_{CIT} = 0.16$$
$$Km_{NAD} = 0.091$$
$$Ki_{NADH} = 0.041$$

akg_n+nad_{nm}+coA_n => $sCoA_n$+$nadh_{nm}$: AKGDHn

$$vf = V_{max}^{KGDH} \frac{akg_n}{akg_n + Km_{AKGD}} \times \frac{nad_{nm}}{nad_{nm} + Km_{NAD}^{KGDH}\left(1 + \frac{nadh_{nm}}{Ki_{NADH}^{KGDH}}\right)} \times \frac{coA_n}{coA_n + Km_{CoA}\left(1 + \frac{sCoA_n}{Ki_{SCoA}}\right)}$$

$$V_{max}^{KGDH} = 134.4$$
$$Km_{AKGD} = 2.5$$
$$Ki_{SCoA} = 0.0045$$
$$Ki_{NADH}^{KGDH} = 0.0045$$
$$Km_{NAD}^{KGDH} = 0.021$$
$$Km_{CoA} = 0.0013$$

$sCoA_n$+adp_n => suc_n+atp_n+coA_n : SCS_n

$$vf = V_{max}^{SCS} \times \frac{sCoA_n}{sCoA_n + Km_{SCS}} \times \frac{adp_n}{adp_n + Km_{ADP}^{SCS}}$$

$$\begin{aligned} V_{max}^{SCS} &= 19200 \\ Km_{SCS} &= 1.6 \\ Km_{ADP}^{SCS} &= 0.25 \end{aligned}$$

fad_n+suc_n => $fadh2_n$+mal_n : SDH_n

$$vf = V_{max}^{SDH} \times \frac{suc_n * fad_n}{suc_n + Km_{SUC}\left(1 + \frac{mal_n}{Ki_{MAL}}\right)}$$

$$\begin{aligned} V_{max}^{SDH} &= 160000 \\ Km_{SUC} &= 1.74 \\ Ki_{MAL} &= 2.2 \end{aligned}$$

mal_n+nad_{nm} => oaa_n+$nadh_{nm}$: MDHn

$$vf = V_{max}^{MDH} \times \frac{mal_n}{Km_{MDH} + mal_n} \times \frac{nad_{nm}}{nad_{nm} + Km_{NAD}^{MDH}}$$

$$\begin{aligned} V_{max}^{MDH} &= 32000 \\ Km_{MDH} &= 0.145 \\ Km_{NAD}^{MDH} &= 0.06 \end{aligned}$$

$fadh2_n$+0.5 O_2^n+2 adp_n => fad_n+2 atp_n : OP1n

$$vf = V_{max}^{OP_1} \times \frac{fadh2_n adp_n O_2^n}{Km_{OP} + fadh2_n adp_n O_2^n}$$

$$\begin{aligned} V_{max}^{OP_1} &= 4.5 \\ Km_{OP} &= 13.48 \end{aligned}$$

$nadh_{nm}$+0.5 O_2^n+3 adp_n => nad_{nm}+3 atp_n : OP2n

$$vf = V_{max}^{OP_2} \frac{nadh_{nm} * adp_n * O_2^n}{Km_{OP} + nadh_{nm} * adp_n * O_2^n}$$

$$V_{max}^{OP_2} = 4.5$$
$$Km_{OP} = 13.48$$

fad_n+$nadh_{nc}$ => $fadh2_n$+nad_{nc} : G3PSn

$$vf = V_{max} \frac{fad_n nadh_{nc}}{Km * Km + Km * fad_n + Km * nadh_{nc} + nadh_{nc} * fad_n}$$

$$V_{max} = 16$$
$$Km = 0.6$$

atp_n => adp_n : ATPaseN

$$vf = V_{max}^{ATPaseN} \times \frac{atp_n}{Km_{ATPase} + atp_n}$$

$$V_{max}^{ATPaseN} = 0.12$$
$$Km_{ATPase} = 0.1$$

atp_a => adp_a : ATPaseA

$$vf = V_{max}^{ATPaseA} \times \frac{atp_a}{Km_{ATPase} + atp_a}$$

$$V_{max}^{ATPaseA} = 0.02$$
$$Km_{ATPase} = 0.1$$

pyr_a => : Mito1

XX

$$vf = V_{max}^{Mito1} \times \frac{pyr_a}{Km_{Mito1} + pyr_a}$$

$$V_{max}^{Mito1} = 0.277$$
$$Km_{Mito1} = 0.2$$

$nadh_a$ => nad_{ac} : G3PSa

$$vf = V_{max} \times \frac{nadh_a}{Km + nadh_a}$$

$$V_{max} = 16$$
$$Km = 0.6$$

adp_a => atp_a : Mito2

$$vf = V_{max}^{Mito2} \times \frac{adp_a}{Km_{Mito2} + adp_a}$$

$$V_{max}^{Mito2} = 4.6$$
$$Km_{Mito2} = 13.48$$

3 P-VALUES

3.1 *Burst mode*

Frequency (Hz)	100	200	400	600	800	1000
Amplitude NADH	0.27	0.23	0.52	0.36	0.26	0.055
FAD	0.63	0.86	0.2	0.39	0.068	0.023
Integral NADH	0.23	0.009	0.09	0.12	0.029	0.009
FAD	0.25	0.003	0.023	0.29	0.66	0.053
Time NADH	4.36e-04	4.66e-03	1.37e-06	7.94e-07	2.05e-04	1.52e-04
FAD	1.7e-05	3.08e-04	5.23e-07	3.48e-07	6.26e-02	0.26

Table 1: Comparison of 400 stimuli with continuous and burst stimulation *p-Values of a two-sided t-test for different parameters*

3.2 *Block of OxPhos*

	Control	Washout
Block NADH	0.0015	0.0654
FAD	0.0001	0.007
Washout NADH	0.0089	-
FAD	0.0035	-

Table 2: Blocking of OxPhos *p-Values of a two-sided t-test to compare the amplitude with an unblocked control and the amplitude after the washout with those during the block.*

3.3 *Increased glucose concentration*

Frequency (Hz)	10	50	100	200	400	600	800	1000
Amplitude NADH	0.2	0.3	0.38	0.6	0.09	0.2	0.16	0.17
FAD	0.06	0.028	0.017	0.222	0.006	0.007	0.019	0.228
Overshoot NADH	0.04	0.0003	0.003	0.002	0.01	0.01	0.01	0.2

Table 3: Comparison of 400 stimuli with in 2mM and 10mM ACSF *p-Values of a two-sided t-test for different parameters*

Figure 1: Paired t-test with bonferoni correction. *Here it is shown how different the amplitudes of two frequencies are. This was done for NADH and FAD with all stimulation paradigms shown above. All values were rounded to the* 5^{th} *decimal place.*

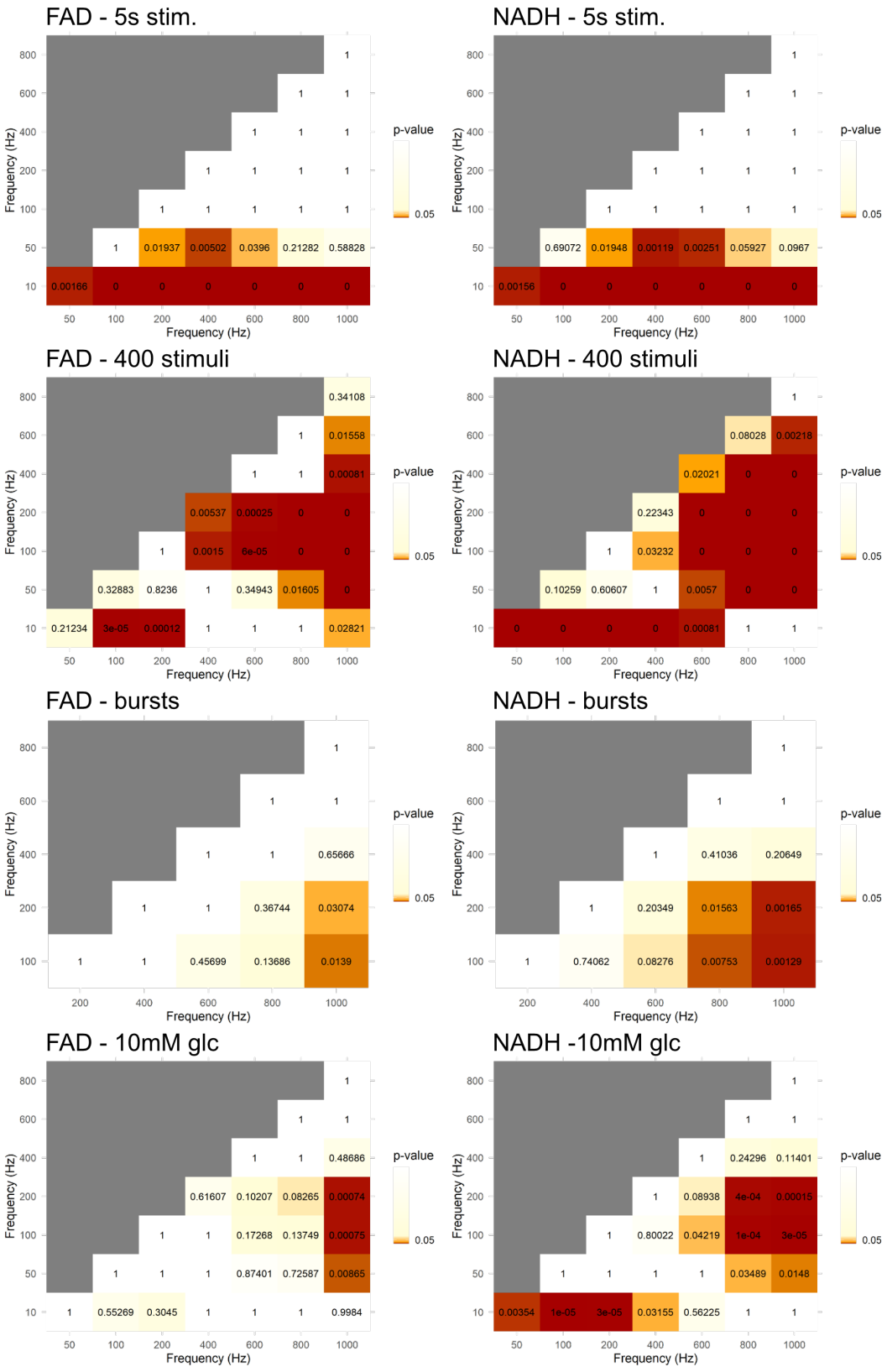
FAD - 5s stim.
NADH - 5s stim.
FAD - 400 stimuli
NADH - 400 stimuli
FAD - bursts
NADH - bursts
FAD - 10mM glc
NADH -10mM glc
Frequency (Hz)
p-value
0.05

LIST OF FIGURES

ACKNOWLEDGEMENTS

First of all I want to thank my supervisor Lars Kunz for all the support he gave me in the last years. His never ending optimism, his advice and guidance helped me to through my PhD. Also when I struggled he always saw something good and reassured me to believe in myself.

Thanks to Thomas Nägele for all the help with the mathematical model. I could have not achieved anything with the model without his expertise and advice.

Thanks to my TAC members Hans Straka, Martin Stemmler and Conny Kopp-Scheinpflug. The input and suggestions during the TAC-meetings were always helpful.

I also want to thank Otto Albrecht who showed me how to do the preparation of the brain slices and where to place the electrodes, also we had great discussions together during our breaks. Also thanks to Hilde Wohfrom for her support and expertise in immunohistology and morphology.

Thanks to Rebbecca, Laurin and Magdalena for the support during wonderful and important coffee and lunch breaks, and also thanks to Santosh for the awesome time in the office with great discussions.

Finally thanks to Chris, Laurin, Franzi and Santosh, who took the time to give me feedback on my thesis. Especially thanks to Nico for all the hours working with me on a good design for presentations, posters or figures and for always supporting me emotionally.

PUBLICATIONS AND AUTHOR CONTRIBUTION

Publication under Revision:
Nicola Palandt[1], Cibell Resch, Patricia Unterlechner, Lukas Voshagen, Valentin Winhart[1], Lars Kunz, (2023) "Metabolic adaptation of auditory neurons to their broad range of action potential frequencies"

[1] affiliated to Graduate School of Systemic Neuroscience (GSN), LMU

Project 1:
The first project was a collaboration of Nicola Palandt (NP), Lars Kunz (LK), Cibell Resch (CR), Patricia Unterlechner (PU), Lukas Voshagen (LV) and Valentin Winhart (VW):

NP and LK designed the study. NP performed most of the experiments. CR performed the experiments on different glucose concentrations. PU and LV conducted experiments on different treatment regimes. VW carried out pharmacological experiments. NP wrote all necessary scripts. NP and LK analysed and interpreted the data. NP did the statistical analysis.

My contribution in detail:

I designed the study together with Lars Kunz, performed the experiments with 5s continuous stimulation and supervised all other experiments. I wrote all scripts that were necessary to achieve a simultaneous measurement of NADH and FAD and to extract the parameters from the raw data. I analysed and interpreted the data and made all figures.

Project 2:
The second project was a collaboration of Nicola Palandt (NP), Cibell Resch (CR) and Lars Kunz (LK):

NP and LK designed the study. LK and NP performed the injections. NP and CR performed the experiments. NP and CR did the immunohistology.

My contribution in detail:

I designed the study and did the systemic injections together with Lars Kunz. I modified the setup to make the measurements of FRET possible. I performed a few of the experiments and supervised the rest. I wrote the script to correct the bleaching and to extract the curves from the videos. I did parts of the immunohistochemistry.

Project 3:
The third project was a collaboration of Nicola Palandt (NP), Lars Kunz (LK) and Thomas Nägele (TN):

NP and LK designed the study. NP implemented the model and performed the first tests. TN and LK supervised the work. NP, TN and LK interpreted the results.

My contribution in detail:

I implemented the models, I performed all tests, I did the sensitivity analysis, I did all figures, I interpreted the results.

Nicola Palandt

Lars Kunz

AFFIDAVIT

Eidesstattliche Versicherung/Affidavit

Hiermit versichere ich an Eides statt, dass ich die vorliegende Dissertation "Metabolic Adaptations to neuronal activity in the Medial Nucleus of the Trapezoid Body" selbstständig angefertigt habe, mich außer der angegebenen keiner weiteren Hilfsmittel bedient und alle Erkenntnisse, die aus dem Schrifttum ganz oder annähernd übernommen sind, als solche kenntlich gemacht und nach ihrer Herkunft unter Bezeichnung der Fundstelle einzeln nachgewiesen habe.

I hereby confirm that the dissertation "Metabolic Adaptations to neuronal activity in the Medial Nucleus of the Trapezoid Body" is the result of my own work and that I have only used sources or materials listed and specified in the dissertation.

München, 27.04.2023

Nicola Palandt